Morphology and topology of dolostone lithons in the regional Carboneras Fault Zone, Southern Spain

Igbokwe, Onyedika A.; Mueller, Mathias; Bertotti, Giovanni; Timothy, Jithender J.; Abah, Obinna; Immenhauser, Adrian

DOI
10.1016/j.jsg.2020.104073

Publication date
2020

Document Version
Accepted author manuscript

Published in
Journal of Structural Geology

Morphology and topology of dolostone lithons in the regional Carboneras Fault Zone, southern Spain.

Onyedika Anthony Igbokwe[1, 2, *], Mathias Mueller[1], Giovanni Bertotti[3], Jithender J. Timothy[4], Obinna Abah[5], Adrian Immenhauser[1],

Affiliation:

[1] Ruhr-University Bochum, Institute of Geology, Mineralogy and Geophysics, Universitätsstraße 150, 44801 Bochum, Germany.

[2]Alex Ekwueme Federal University Ndufu-Alike, Ikwo, Department of Physics, Geology and Geophysics, P.M.B. 1010, Abakaliki, Ebonyi State, Nigeria.

[3]Delft University of Technology, Faculty of Civil Engineering and Geoscience, Stevinweg 1, 2628 CN Delft, Netherlands.

[4]Ruhr University Bochum, Institute for Structural Mechanics, Universitätsstraße 150, 44801 Bochum, Germany.

[5]Queen's University Belfast, School of Mathematics and Physics, University Road, Belfast, BT7 1NN, Northern Ireland, U.K.

* Corresponding author. Email: onyedikachi.igbokwe@rub.de

Keywords:

Lithons; Dolostone; Background deformation; Topology; Carboneras Fault Zone; Fracture network connectivity.

ABSTRACT

Dolostones in a Neogene strike-slip fault zone are described. Two main types of structural features are recognised: (i) Background deformation in the form of a network of bedding-perpendicular and hybrid conjugate fractures, barren fractures and bedding-parallel stylolites. (ii) Fault-related features include breccias and cataclasites. Orthorhombic rock lithons are generated from the intersection of fracture sets with bedding and/or joints. Lithon size and morphology change across the dolostone fault block gradually producing a tetragonal or isometric shape. The lithons are 1 – 2 cm in dimension (only ~ 20% outside this range) and have an average cross-sectional aspect ratio of 1.6, irrespective of size or structural position. Topology is analysed using nodes and branches, ranging from isolated (I- node and I-I branch) to connected (Y- and X- nodes, and I-C to C-C branches) respectively. The quantitative description of the geometrical and topological analysis of the dolostone lithons suggest that they become more connected and interact within the dolostone fault blocks. Assessing the change in topology and lithons connectivity have important implications for subsurface reservoirs and aquifers hosted in dolostone-fault zones.

1. Introduction

Faulting largely takes place in the Earth's uppermost crust at varied confining pressures, and propagates by the formation and/or reactivation of mesoscopic joints (Segall and Pollard, 1983; Pollard and Fletcher, 2006). When carbonate rocks are involved in faulting, structural elements including fracture (joint and small-scale fault) networks, pressure solution seams, compaction and shear bands are predominant (Billi et al., 2003; Agosta et al., 2009), and these structures have different effects on subsurface fluid flow, which may induce dolomitization, dedolomitization or any other form of alteration (Aydin, 2000; Sibson, 2000). For instance, joints as opening-mode fractures (Pollard and Aydin, 1988; Peacock et al., 2016), form efficient pathways along which fluids circulate, whereas the compaction bands are perceived to restrain the fluid flow in relation with the surrounding porous rocks (Tondi, 2007; Agosta et al., 2009). On the other side, pressure solution as closing-mode fractures (stylolites; Fletcher and Pollard, 1981) and shear bands (depending on their mechanical processes) may channel fluid flow when these elements are sheared (Caine et al., 1996; Jourde et al., 2002).

In fault zones, deformational features are associated with slip surfaces, shearing and heterogeneous strain distribution over a wide range of scales (meters to kilometers; Shipton and Cowie, 2003; Agosta et al., 2012; Choi et al., 2016). The different components (e.g., host-rock, damage zone and fault core) and their geometric characteristics have been well established (for example, Segall and Pollard, 1983; Chester and Logan, 1986; Kim et al., 2004; Agosta and Aydin, 2006; Childs et al., 2009; Choi et al., 2016). In essence, a mature fault zone is made up of two main structural zones: (i) the fault core, where most of the displacement is accommodated, and (ii) the corresponding damage zone, which is mechanically related to the growth of the fault zone (Chester and Logan, 1986; Caine et al., 1996). The fault core is often composed of a fault gouge, a breccia and/or a cataclasite (Sibson, 1977; Caine et al., 1996; Billi et al., 2003; Agosta and Aydin, 2006). There, the pre-existing sedimentary and tectonic structures are commonly obliterated. In the damage zone, fault-related fracture networks crosscut the country rock and the bedding planes and inherited structural fabrics, including numerous fractures and/or small-scale faults that do not obliterate the host rock fabrics, may be preserved to variable degrees. The relative volumetrical percentage of fault core and damage zone structures, and the inherent variability in grain scale and fracture permeability play a pivotal role as to whether a fault zone will act as a conduit for fluids, as a barrier, or as a combined conduit-barrier system (Caine et al., 1996; Jourde et al., 2002). Both the fault core and damage zone are bounded by the hostrock, which is generally characterized by background tectonic structures due to previous deformation. Increased deformation and disaggregation of these rocks in fault zone lean towards the formation of mosaic breccia and/or cataclasites. The formation of mosaic breccia requires a volume change. Mosaic breccias are made of a type of fault rock that has its fragments largely, but not completely disjointed and displaced (Mort and Woodcock, 2008). Moreover, typical fault zone facies are cataclasites – a cohesive granular fault rock, which contain finer fragments in relation to breccias (Agosta and Aydin, 2006; Mort and Woodcock, 2008; Peacock et al., 2016).

Despite a significant amount of published work (Doblas et al., 1997; Billi et al., 2003; Billi, 2005; Agosta et al., 2009; Bisdom et al., 2016 and references therein), uncertainty still exists with regard to our understanding of morphological changes of the deformed carbonate hostrock clast ('lithons'). An improved knowledge of the morphological evolution of lithons is thus essential to understand their connectivity and patterns over time.

Additionally, in deformed carbonate, fractures have non-random orientations (intersecting at approximately 90 +/- 20^{o}) and form nearly orthorhombic lithons (i.e. three mutually perpendicular symmetry axes, all of different lengths). Clearly, in order to understand the morphological evolution of lithons in carbonates, fracture patterns and fracture networks connectivity, their geometrical, kinematic and topological properties must be considered. Several studies of the fracture networks and their patterns have focused on the geometrical and kinematic parameters of individual fractures (Nixon et al., 2014; Peacock et al., 2016). These are limited, however, as both parameters do not fully consider the arrangement and relationships between fractures and the network topology. Topology defines and quantifies the different spatial relationships between fractures, focusing on fracture termination, intersections, network connectivity and flow properties

(Sanderson and Nixon, 2015, 2018; Morley and Nixon, 2016; Duffy et al., 2017). Topological properties have not been previously considered for rock lithons in fault damage zone. Therefore, an improved knowledge of the (lithons) network connectivity and the complexity is crucial for the understanding of fluid flow through a given carbonate rock. Moreover, a topological characterization offers a more direct route to determine connectivity and percolation potential of a fracture network when compared to geometric characterization (Sanderson and Nixon, 2018; Dimmen et al., 2017).

The aim of this paper is to provide a quantitative geometrical, topological and structural characterisation of large (meter-sized) blocks of dolostones formed by well-preserved lithons within a regional fault zone (Carboneras Fault Zone, Southern Spain), which was active since the Early Miocene (Fig. 1). An area about 4.5 km-long and up to 1 km-wide (Figs. 1b and 2a) provides data that are placed in the context of the deformation history and characteristics of these large dolostone blocks. Dolostone blocks are differentiated with respect to the degree of deformation, ranging from the relatively undeformed host rock (accommodating diffuse deformation) to intensely deformed dolomitic breccia. The background deformation of dolostones and their associated range of burial depths are discussed. Fractures/faults network connectivity, including other brittle structures, and the resulting patterns of lithons are quantified, visualized and discussed in terms of geometry and topology.

The results of this study have several important implications, inasmuch as they provide: (i) constraints on the lithon morphology of carbonates; (ii) evidence on the quantification and visualization of the complex fracture connectivity, and fluid flow in fault zones; and (iii) estimates of the geometrical and topological variability of dolostone lithons in the fault zone. All of these aspects are significant for a wide range of fundamental and economic applications.

2. Terminology

Structurally, the terminology defined by Billi et al. (2003), Agosta and Aydin, (2006) and Peacock et al. (2016) was applied but is here used more specifically: (i) *Lithon* describes a deformed hostrock clast created from the intersection of fracture sets with bedding and/or joints (Fig. 2b and c; Billi et al., 2003). (ii) *Lithons' blocks* refer to dolostone blocks where bedding is still visible and affected by distributed orthogonal fractures and stylolites forming lithons (Fig. 2b). These blocks are relatively undeformed when compared with intensely deformed fault blocks. (iii) *Fault blocks* refer to dolostone blocks affected by pervasive orthogonal (barren) fractures forming lithons and accommodating a localized fault zone (damage zone and fault core; Fig. 2c). All of these blocks (lithons' and fault blocks being cm's up to tens-of-meters in size) are essentially transported, meaning that the blocks are dislocated by, and have experienced significant rotation inside, the Carboneras Fault zone. (iv) *Fractures* form the boundaries of lithons and are part of the damage zone of small-scale faults with sub cm-scale of displacement. Specifically, for the use in the topological analysis, fractures include both joints and faults. This usage was required due to the challenging approach to distinguish between these features at the sub cm-scale.

Some fractures are filled with dolomite cements (veins), which are microscopically distinguished in cement phases as Dol. 1 – 3. These refer to: (i) homogenous microcrystalline dolomite cements (Dol. 1), (ii) coarse crystalline dolomite cements (Dol. 2), and (iii) paragenetically young dolomite cements (Dol. 3).

3. Regional geological setting

3.1. Geotectonic setting of Southeastern Spain

The Carboneras fault zone (Fig. 1) forms part of the Trans-Alboran shear zone, which constitutes a major NE-SW trending sinistral strike-slip fault system of the Betic Cordillera, active since the Neogene (De Larouzière et al., 1988). This fault zone is 150 km-long and up to 1 km-wide, and predominantly moved between 12 and 6 Ma (Faulkner et al., 2003, 2008; Rutter et al., 2012, 2014). The Trans-Alboran shear zone system comprises the Alhama de Murcia, Palomares, and Carboneras faults, and cuts across several structural nappes of the Betic Cordillera (Fig. 1a; Keller et al., 1995, 1997). The Betic Cordillera, an ENE-WSW trending Alpine orogenic belt, is divided into an unmetamorphosed External Zone in the north and a metamorphic Internal Zone towards the south. The External Zone is composed of Mesozoic sedimentary rocks, mostly limestones that unconformably overlie the Iberian massif. These are deformed by middle to late Miocene thrusting and folding with a NW-SE shortening direction. On the other side, the Betic Internal Zone comprises metamorphic and sedimentary rocks of Paleozoic to Cenozoic age exposed in elongated ranges. These are separated by intramontane basins filled by continental and marine sediments of Neogene and Quaternary age (Fig.1b; Frizon et al., 1991; Morales et al., 1999; Visser et al., 1995; Alonso-Chaves et al., 2004 and references therein). In addition, the Internal Zone constrains a large number of stacked thrust sheets (tectonic units) grouped into three nappe complexes: (i) the Nevado-Filabride, (ii) the Alpujarride and (iii) the Malaguide complex (Alonso-Chaves et al., 2004). The Nevado-Filabride units are overthrusted by the Alpujarride and both are exposed within the basement high of Sierra Carbrera and the Sierra Alhamilla, respectively (Fig. 1). Nevado-Filabride and Alpujarride nappe complexes are characterized by upper greenschist facies, mica schists and quartzites (Nevado-Filabride), as well as by phyllites and dolostones of Triassic age (Alpujarride; Kampschuur and Rondeel, 1975; Keller et al., 1995; Faulkner et al., 2003).

The Malaguide units are largely unmetamorphosed and built by Palaeozoic shales and sandstones, Permo-Triassic red sandstones and shales (Kampschuur and Rondeel, 1975; Frizon et al., 1991; Keller et al., 1995; Visser et al., 1995; Morales et al., 1999; Alonso-Chaves et al., 2004 and references therein).

The Carboneras Fault was inferred to have an offset of ~ 40 km, an average slip-rate of 2.7 mm/year (Faulkner et al., 2003; Rutter et al. 2012), and separates the volcanic Cabo de Gata province to the south from the uplifted Alpine metamorphic basement blocks and Neogene basins to the north (Fig. 1b; Rutter et al., 2012, 2014). The various lithologies in the large-scale fault zone are well-exposed under the present-day semi-arid climate. Further details on the stratigraphy, tectonics, style of deformation, strain distribution, and the structural evolution of the Carboneras fault zone were discussed in Kampschuur and Rondeel (1975), Keller et al. (1995, 1997), Faulkner et al. (2003, 2008), Alonso-Chaves et al. (2004) and Rutter et al. (2012, 2014 and references therein).

3.2. Deformed lithologies in the Carboneras Fault Zone

The different rocks types (lithologies) within the Carboneras fault zone reveal a combination of both distributed and localized deformation, which are scale-dependent in the constituent fault strands. The fault zone affects allochthonous basement rocks, mainly andalusite-and garnet-bearing graphitic mica schists, phyllites, Messinian evaporites, and Mesozoic dolostones (Faulkner et al., 2003, 2008), all embedded in multiple strands of a clay-bearing fault gouge (Figs. 2a, 3a and b). The distributed deformation is accommodated in the phyllosilicate-rich fault gouge, whereas the localized deformation is constrained within the variably fractured dolostones and/or mosaic breccias. The focus is on dolostone blocks that range between some centimeters and tens-of-centimeters in dimensions. The localization of the deformation in the dolostones contrasts with the style of deformation in the phyllosilicate-rich gouges. The dolostones are deformed with profuse fault surfaces and fracturing that breaks the dolostone blocks into centimeter to decimeter-sized lithons commonly in cube-like shapes (Fig. 3). Locally, dolostones show a high degree of faulting and hydrothermal overprint.

4. Material and methods

4.1. Fieldwork

The spatial distribution of dolostones was characterized and mapped along the east west trending segment of the Carboneras fault zone (Figs. 1b and 2a), which is situated outside of the classical field area of Rutter et al. (2012, 2014). This allowed for the identification of dolostone blocks at different scales, their preserved sedimentary features and their style of deformation. Fieldwork focused on: (i) sedimentological and facies interpretation, (ii) description of macroscopic diagenetic features, (iii) mapping of the distribution of fracture-related structures and structural features of fractured dolostones, (iv) qualitative structural analysis of fractures (barren and filled fractures) and (v) quantitative analyses of the structural elements assessing their geometrical and topological relationships between interacting fractures, and their distribution. Representative samples were collected along the fault zone outside of the natural park. Forty samples were selected for thin-section preparation and petrographic analysis.

4.2. Structural analysis and topological parameters

4.2.1. Fracture acquisition and analysis

Fracture analyses were performed in the field on selected dolostone blocks (Fig. 2a). These outcrops form dolostone fabrics ranging from least deformed (background deformation) to such that were intensely fractured (tectonic breccia and fault gouges) in the context of strike-slip tectonics and related hydrothermal alteration. The criteria employed to separate background deformation from deformational features as a result of faulting overprint was essentially the recognition of preserved early diagenetic features in the dolostone lithons' blocks. Investigating the dolostones outside of the fault zone was not feasible as they are only exposed within the fault zone. Outcrops were grouped into the following: (i) relatively undeformed host dolostone with background fracturing; (ii) fault-related dolostone breccia displaying intense fracturing; and (iii) fault gouge and/or cataclasite, with both matrix and clast supported examples forming the 'matrix' of the fault zone.

Fracture data were acquired by direct measurement of fractures in the field and from ortho-rectified images obtained with a Nikon P7800 camera. Over 5000 fractures were mapped. These included veins ranging in length from 0.5 cm to some meters. Scan-lines and scan-area measurements were carried out in different dolostone fault blocks encompassing both the damage zone and the fault core. In each scan-line, detailed structural data to include types of structures and their orientations were recorded to produce stereoplots and other relevant plots. Similarly, attitude, position, crosscutting relationships of the bedding and fractures, and spacing (the distance between fractures measured along a scan line) were measured.

4.2.2. Dimensions of lithons

The dimensions of lithons generated by the intersection of fracture sets from different selected scan-lines were measured. The fractures usually intersect at angles approximately 90 +/- 20º thereby forming lithons that are almost orthorhombic. In some areas, however, the fracture intersection is at a relatively low angle. We computed the 2D aspect ratio (A_r) of 150 measurements of rock lithons for individual scan-line. The aspect ratio is defined by the ratio of the longer (L) to the shorter (l) side of the cube (rectangle) best restraining the section of each lithon. The mean aspect ratio was determined from the A_r. population of each scan-line. We computed the shape factor (S_f) of the lithons from few selected scan-lines Eq. (1), particularly where the outcrops show 3D view of the lithons. The shape factor is the ratio between the long-side of the lithons (L) minus width (W) divided by the width (W) minus the short-side (l). The width is the distance, parallel to the bedding, between two contiguous intersection of adjacent fracture surfaces.

$$S_f = \frac{(L-W)}{(W-l)} \quad \ldots\ldots\ldots\ldots\ldots\ldots\ldots\ldots\ldots\ldots\ldots\ldots \quad (1)$$

S_f defines the shape of the lithon in relation to bedding and fracture orientations (Fig. 3g). We documented the lateral changes in shapes and grain-sizes, from the statistical data of size of the small blocks that can be derived from the images. We also examined the potential of using the spacing, aspect ratio and shape factor to characterize the deformation intensity.

4.2.3. Node and branch topology

Topological characterization was undertaken using a ‘NetworkGT’ toolbox in ArcGIS developed by Nyberg et al. (2018). Topology describes the geometrical relationships of fractures and is used to demonstrate the arrangement of fractures within networks to determine their connectivity (Manzocchi, 2002; Sanderson and Nixon, 2015, 2018). Connectivity refers to: (i) a measure of the degree to which the elements of a network are interconnected; or (ii) a limit or threshold, below which the network is `unconnected´ and above which it is `connected´ (Sanderson and Nixon, 2018). In 2D, the topology of a natural fractured network comprises nodes and branches between nodes (Fig. 4a; Manzocchi, 2002; Sanderson and Nixon, 2015). Depending on their connectivity and geometry, nodes can be classified as: (i) I-nodes denoting isolated tips of a single branch; (ii) Y-nodes characterized with 3 branches; and (iii) X-nodes associated with two crossing fractures that produces four branches. Branches have two nodes at their ends and are divided into three types, based on an isolated (I-) node or a connecting (Y-or X-) node: isolated I-I branches with no connecting nodes; singly connected I-C branches with one connecting node; or doubly connected C-C branches with two connecting nodes (Fig. 4b and c; Sanderson and Nixon, 2015; Duffy et al., 2017). The proportion of different node and branch types described the network topology, and when plotted on a ternary diagram (node and branch triangle) allows for different fractured networks to be assessed.

A total of seven selected outcrops of fractured bound dolostone fault blocks located within the east west trending segment of Carboneras fault zone were investigated. Out of these, three representative outcrops are presented (Fig. 2a; CF 9_11, CF 35 and CF 25). The average number of connections per branch (C_B) describes the degree of connectivity between branches within the network. The values of C_B range from 0 to 2, with value 2 signifying a very highly and/or perfectly connected network (for details of the mathematical derivation see Sanderson and Nixon, 2015).

4.3. Stylolite analysis as a proxy for compressive stress and burial depth

The morphology of stylolites was used in order to estimate: (i) the compressive stress direction; (ii) the burial depth of formation (Bertotti et al., 2017) and (iii) the amount of compaction (Ebner et al., 2009a). These estimates are calculated from the scaling of stylolite roughness (Renard et al., 2004), an approach that was tested in Schmittbuhl et al. (2004) and Ebner et al. (2009b).

A set of five bedding-parallel stylolites were collected within the sample locations marked as CF 2, CF 3 and CF 6 in Figure 2a. The samples were cut normal to the main stylolitic plane and polished. Each slab was scanned with an EPSO Perfection V550 photo scanner and the traces of the stylolites were digitized in GIS environment (QGIS 3.2.1). The Fourier Power Spectra P(*k*) as a function of the wave-number *k* [1/length scale (mm^{-1})] for each stylolite pattern was calculated and plotted to determine the cross-over wavelength between the two self-affine regimes corresponding to the elastic energy dominated regime at large-scale and surface energy dominated regime at small-scale. The cross-over length (*Lc*) gives a value for the causative stress on the stylolite interface and is linked in the equation below.

$\sigma_z = +/- (\frac{3\gamma E}{a\beta Lc})^{1/2}$ ………………(2), where γ is the surface free energy, E the Young modulus, β a function of the Poisson ratio ($\beta = \frac{2v(1-2v)}{\pi}$). To extract values of the vertical stresses and the corresponding depths of stylolite formation, parameters shown in Table 1 were adopted. Values obtained from different samples lead to directly comparable results, a feature that is considered promising. For details of the mathematical derivation see Appendix A1.

5. Results

Depending on the dolostone block studied and the degree of fabric destructive dolomitization, the sedimentological features points to: (i) dolostone facies with dm-thick layering to massive facies with bed thickness of up to one meter (Fig. 5a – c), and (ii) locally massive facies with no discernible bedding features across several meters of dolostone lithons' block. Microscopic observations show that the layered dolostones are formed by two dolomite generations: (i) homogenous, fabric-preserving, microcrystalline Dol. 1 and (ii) coarse-crystalline (crystals up to 1 cm in size) fabrics with characteristically cloudy cores and clear rims (Dol. 2; Fig. 5d, e and h).

Dolostones and bedding parallel stylolites are crosscut by bedding-perpendicular veins filled with paragenetically younger dolomite cement Dol. 3 (Fig. 5f and g).

Background deformations are distinguished as opening mode (veins and/or joints), bedding-parallel stylolites, semi-ductile shear zones, and mixed-mode or hybrid fractures (extension/shear). This deformation also extends to the lithons, which are distributed at low-strain. Features relating to faulting overprint include intense breccias and cataclasites (Fig. 6a – c). These features are differentiated based on the degree of faulting overprint and hydrothermal alteration. Breccias and cataclasites usually contain Dol. 1 through 3 clasts, evidencing that they originated from the same host rock dolostone. Microscopic differentiation of breccias in the cataclasite matrix provide evidence for brecciation predating cataclasation (Fig. 6d - g; see Appendix A2 for detailed microstructural description).

5.1. Structural features relating to the background deformation.

The structural elements of the background deformation are characterized in figures 7 through 9. The contractional fractures (bedding-parallel stylolites) present within individual dolostone strata enhance bedding planes. Usually, these stylolites display well-developed peaks (Figs. 7a and 8d) and commonly connect with each other within the same bed. Sometimes, individual bedding-parallel stylolites extend over 80 cm and the vertical spacing between these features is on the order of a few centimeters to tens-of-centimeters.

In figures 7c and 8a, the blocks of dolostone display a localized deformation in a narrow semi-ductile shear zone. The semi-ductile shear zones are characteristically organized in conjugate patterns, and their directions are assumed from the biaxial intersection plane of the two conjugates.

The opening mode fractures, here veins, are occluded by various cement phases that can either be dolomitic or calcitic in terms of their mineralogy (Fig. 5b - g). Field observations show that veins generally range from near-perpendicular to bedding to, less commonly, oblique (oriented 40 to 65 degrees) relative to bedding. Veins are several centimeters long (0.5 – 7.5 cm) and can be few millimeters to some tens of centimeters in width (1 – 15 mm; Figs. 5b, f, and 9a). The veins spacing range from 0.4 – 4 cm (Fig. 9d). Veins with widths of less than 1.5 mm characteristically exhibit matching opposing walls. In contrast, veins with widths of several mm may show opposing walls that do not match in terms of their morphology. Veins perpendicular to bedding are either stratabound or non-stratabound. For a selected pavement (Fig. 9a), three main vein sets were identified (set 1 through 3; Fig. 9b and c). The chronological order is established based on crosscutting relationships. Field observations show vein set 1 and 2 are coeval, then followed by 3.

Other dolostone blocks (Figs. 7 and 8) show veins occurring in a left-stepping and right-stepping en échelon pattern, which are regular, systematic and well organised in conjugate sets. The en échelon conjugate veins are roughly parallel to each other and nearly perpendicular to bedding with a shear component reflected by tension – gashes. The tension gashes usually show planar and incipient sigmodial Z- and S-shapes. The dihedral angles exhibited by the conjugate align between 15 and 60^{o}. Commonly, en échelon veins are: (i) formed within the semi-ductile shear zones and (ii) overprinted by bedding-parallel stylolites, terminate against bedding-parallel stylolites and/or against the bedding surfaces (Figs. 7 and 8).

Later bedding perpendicular veins (Fig. 7c), are less regular and less organised but are elongate, abundant and usually bisect the shear boundaries in the vicinity of the conjugate veins. These are filled by Dol. 3 cements. Most of these veins are reactivated, leading to barren fractures (joints) that follow almost the same orientation as the veins. The statistical description and spacing distribution show that most of the vein sets are largely clustered.

5.2. *Burial depth of formation of bedding-parallel stylolites*

The results from the Fourier Power Spectra P(*k*) analysis of the morphology of the bedding-parallel stylolites are presented in Figure 10. Average crossover lengths, estimated wave numbers and corresponding estimated vertical stresses from equation (2) are documented in Table 2, along with calculated depths. The values range from 10 – 17.6 MPa (440 – 820 m). Uncertainties in input parameters, e.g., Young's Modulus, surface energy and Poisson ratio impact on the calculated stress. For the depth estimation from the stress, the values are dependent on the: (i) overburden density and (ii) assumption that the stress is isotropic in the horizontal plane, which is debatable at depth in a complex tectonic context (Beaudoin et al., 2016).

5.3. *Structural complex zone and Lithons' distributions in the dolostone fault blocks*

Field observations towards the NW reaches of the east west segment of Carboneras fault zone show outcrops that are structurally complex and there fracture frequencies are particularly high, and a wide variation of fracture orientation is observed. These outcrops show the distribution, geometrical and morphological representation of lithons in individual blocks (Figs. 3c through f and 11a). Several of these lithons show crushed surfaces and evidence of significant rotations. Their spacing distribution and/or descriptive statistics are shown in Figure 11d through i, and in table 3.

The 1500 measured lithons in the dolostones mostly comprises lithons of 0.05 – 14 cm in short-side (*l*), with long-side (*L*) varying from 0.1 – 17 cm (Fig. 12a, d and e). Figure 12b and c show the histogram of the aspect ratio of the overall and selected scan-lines respectively. The aspect ratio varies between 0.2 and 48.5, and the overall distributions of these aspect ratio distinctly show lithons of variable sizes within the selected scan-lines. The geometrical analysis and statistical descriptions of the lithons sizes (within the selected lithons' and fault blocks) give a mean aspect ratio (mAr) value of 1.6 (standard deviation σ = 1.5; Fig. 12a – e). The shape factor (S_f) predicts the shape of the lithons, and ranges from 0 to 1, with value 1 pointing to a shape of all equal dimensions.

Figure 13 shows the variations in the size of the lithon's fragments in a scan-line of dolostone fault block (CF11c). The change in size and shape is marked by the reduction of the lithon's sizes, which can be quantified from the measurement of lithon's diameter ($\sqrt{L * l}$), aspect ratio and shape factor. Figure 13a plots histogram distribution of shape factor. The range of S_f values, from 0.34 to 0.99 with an average of 0.78, point to a varied lithon shape across the transect. The lateral change of size and shape reduction of lithons reaches about 20% (Fig. 13a). The lithons show a great deal of variation in their diameter and aspect ratio, and the transition in the context of the diameter measurement of each of the lithons, are overtly continuous.

Other selected scan-lines show irregular size distributions (Fig. 12c). In places where the boundary fault surface is between the damaged zone and fault core in a fault block, the lithons usually change their size and shape abruptly, especially as the lithons are located more closely towards the fault gouge.

5.4. Fracture geometry and topological characteristics of the structural complex zones

The studied fractures in the dolostone fault blocks display a variable degree of structural complexity. This complexity is evident where two or more fractures segment, intersect, splay, cross-cut or abut against another. The digitized fracture network, fracture intensity maps, connecting node frequencies, distribution analysis of fracture lengths using a series of cumulative frequency plots and a table of statistics of the geometry of the selected fracture network are displayed in Figures 14, 15 and 16. Table 4 shows the proportion of the node and branch data derived from the fractured network of outcrops CF 9_11, CF 35 and CF 25. Given that the spatial relations and geometry between different structures are constrained, three representative outcrop examples were chosen and described due to their relative representation of fracture topology and connectivity based on fracture intersections.

Outcrops CF 9_11, CF 35 and CF 25 are located within the east west branch of Carboneras fault zone as shown in figures 1b and 2a. While outcrop (CF 9_11) is in the NE side, outcrops (CF 35) and (CF 25) are localized in the NW reaches of the area. These outcrops are limited to a ~1, 2.5 and 1.5 m portions of localized damaged zone of the dolostone fault blocks, and are divided into sectors based on the degree of fracture intensities respectively (Figs. 14d, 15d and 16d). Given that the blocks analysed in Figures 14, 15, 16 are from the fault zone and hence may be rotated blocks, the topology would still have meaning, but the orientation of the sets may have little significance.

For outcrop CF 9_11; the fracture network consists of a predominant set 1 (red) and a set 2 (blue) fractures (Fig. 14b, f). The set 1 and 2 fractures are sub-parallel, overlapping, and regularly spaced on the order of 0.5 – 2 cm and 0.1 – 2 cm spacing respectively. Both fracture sets are pervasive and the set 1 intersect at nearly orthogonal with the set 2.

For outcrop CF 35; the fracture network comprises: (i) a predominant set 1 (red), (ii) set 2 (blue) and (iii) set 3 (black) fracture sets (Fig. 15b). Most of the set 1 and 2 fractures form conjugate pairs and usually crosscut each other. In some instances, these fractures are either isolated or abut against the set 3 fracture sets. In addition, set 1 through 3 fracture sets are sub-parallel, overlapping and regularly spaced on the order of 0.8 – 2.5 cm, 1 – 3 cm and 0.5 – 2cm spacing respectively.

For outcrop CF 25, the fracture sets are dominated by set 1 (red), set 2 (blue) and set 3 (black) fracture sets (Fig. 16b, f). The set 2 and set 3 fractures are sub-parallel, overlapping, sometimes abut against each other, and somewhat irregularly spaced. The set 1 exhibit a more regular spacing, commonly form in conjugate pairs with set 2, and mutually cross-cutting each other. All the fracture sets are moderately pervasive.

The fracture networks of all outcrops appear to have a very high degree of connectivity based on the intersections among themselves, displaying a distinctive cubic-to-near-rectangular shape configuration (lithons). The structural configurations of the fracture networks of the individual dolostone fault blocks are captured by nodal and branch topologies. We documented the abundance of abutting, splaying and many cross-cutting interactions in the network linked with Y- and X- nodes, and I-C or C-C branches (Figs. 14c, 15c and 16c). The proportion of Y- and X- nodes and number of connection-per-branch (C_B) documented in all the outcrops (CF 9_11, CF 35 and CF 25) respectively are as follows: (i) 74.6%, 19.3% and 1.9, (ii) 56.1%, 18.6% and 1.8. (iii) 49.9%, 16.0% and 1.7 (Table 4; Figs. 14h, i, 15h, i, and 16h, i). The structural complex zones show higher fracture intensities (Figs. 14d, 15d and 16d), and higher frequencies of connecting nodes (Figs. 14e 15e, and 16e). The higher fracture intensities sustain a good correlation with connecting node frequencies.

6. Data interpretation and discussion

The documented structural data in the dolostone blocks were interpreted considering not only their mode, kinematics, orientation, abutting and cross-cutting relationships for the different structural elements, but also the results of previous works carried out in similar rocks. For this reason, we discuss the background (diffuse) deformation that took place at the initial stage of the dolostone deformation separately. We then qualitatively and quantitatively explain the nucleation, evolution and morphology of dolostones lithons, focusing on their geometry, topology, and their significance in term of fluid flow properties in the subsurface.

6.1. Background deformation in the lithons' block

Deformation in the dolostones of Carboneras fault zone prior to faulting overprint caused the development of different sets of structures, to include conjugate semi-ductile shear zones, conjugate en échelon fractures (veins), bedding-perpendicular veins, joints and bedding-parallel stylolites. These structures form the background deformation of the study dolostones and are displayed in different selected dolostone lithons' blocks (Figs. 7 through 9). As documented before, these structures are low-strain fractures and can form during subsidence/burial diagenesis (Larsen et al., 2010; Lamarche et al., 2012; Korneva et al., 2014; Lavenu et al., 2014; Bisdom et al., 2016; Bertotti et al., 2017) and/or at the initial stages of faulting activities (Agosta and Aydin, 2006; Tondi, 2007; Agosta et al., 2009). In dolostone blocks, hybrid conjugate en échelon veins: (i) predate most of the structural elements (including bedding-parallel, bedding-perpendicular and oblique fractures), (ii) form inside the conjugate semi-ductile shear zones of the lithons' blocks (Fig. 7 and 8a), (iii) exhibit apparent symmetry between the veins sets and (iv) display lack of consistent cross-cutting relationships between the different kinematic indicators. All these characteristics infer that these conjugate en échelon veins do not form during distinct tectonic events, and point to a conjugate vein system that is kinematically and geometrically related. Besides, these veins are largely overprinted by bedding-parallel stylolites (Figs. 7a and 8d). In other places, conjugate sets of en échelon veins have been documented in the localized ductile shear zones in the White Range, central Australia (Ramsay, 1980; Kirschner and Teyssier, 1994), in the southern margin of the Bristol Channel, North Somerset, UK (Belayneh and Cosgrove, 2010), Berda and Kef Eddour formations in Tunisia (Bisdom et al., 2016), and the Jandaira Formation in Brazil (Bertotti et al., 2017). In these aforementioned places, conjugate en échelon veins disrupt the ductilely formed fabrics, intersect roughly perpendicular to bedding, show dihedral angles < 30^{o} and are thought to have formed during early horizontal contraction. These published examples share some of the characteristics of those observed in the dolostone lithons' blocks within Carboneras fault. Therefore, conjugate en échelon veins are thought to develop not only due to burial and/or subsidence but also may form during early horizontal contraction, possibly due to high fluid pressures that overcame the vertical loading (Srivastava and Engelder, 1990) and/or local stress perturbations (Lavenu et al., 2014).

The overprinting relationships between the bedding-parallel stylolites (resulting from closing mode failure occurring perpendicular to the greatest principal stress, Fletcher and Pollard, 1981),conjugate semi-ductile shear zones and en échelon veins (resulting from opening mode failure occurring perpendicular to the least principal stress, Pollard and Aydin, 1988), indicate both a gradual shift between the main and the least principal stresses as well as a non-synchronous deformation event at the initial stage. These processes have been explained with the concept of mechanism of stress relaxation, reloading and/or perturbations in Agosta and Aydin, (2006) and Bertotti et al. (2017). In essence, burial of the dolostone lithons' block followed an initial deformation stage (at shallow depth) that caused the formation of conjugate semi-ductile shear zones, which accommodate the bedding-perpendicular conjugate en échelon veins, before the formation of bedding-parallel stylolites with increasing depth. This is consistent with the deformation regime associated to a stress field documenting sub-vertical principal stress σ_1 and sub-horizontal σ_2.

The dolostones were buried to depths of 440 – 820 m (Table 2; Fig. 10). This range depicts the minimum depth at which the dissolution was active on the bedding parallel stylolite planes and is consistence with the local burial pathway (Mueller et al., 2020). Some fractures were interpreted to have formed after stylolitization. These fractures, filled with late diagenetic dolomite cement, (Dol.3) are largely bedding-perpendicular and nucleated as veins overprinting the stylolites. The reader is refered to Mueller et al. (2020) for an in-depth documentation of the full paragenetic sequence, burial temperature and age constraints involved in the complex burial history of these dolostones.

6.2. The characteristics and evolution of lithons' blocks

6.2.1. The morphological and geometrical evolution

The cross-orthogonal sets of fractures (joints) in the dolostones blocks generated rock lithons that are orthorhombically arranged in well-connected discontinuities, which have obviously impacted on the original isotropic character of the dolostones. Orthorhombic lithons generated by one set of joints could be fractured in an orthogonal direction forming the second set of joints (Figs. 2 b - c, 3f and 17 a - c; Billi et al., 2003; Billi, 2005). These orthogonal fracture sets (related to the genesis of lithons) clearly indicate tectonic events that postdate the background deformation including conjugate en échelon veins and stylolite generation.

In brittle fractures and faults, the orthorhombic arrangement was first proposed in Oertel, (1965), and was later extended to include brittle-ductile zones of localized displacement in Kirschner and Teyssier (1994). These orthorhombic structures are thought to develop during bulk non-plane-strain (triaxial) deformation where three or more mutually cross-cutting fault and/or fracture sets develop contemporaneously (Oertel, 1965; Reches, 1983; Reches and Dieterich, 1983; Kirschner and Teyssier, 1994). Moreover, orthorhombic structures are predominant in carbonate platforms that have suffered successive deformation. Turcotte and Schubert (2002), Billi et al. (2003) and Billi (2005) have elucidated the orthogonal fracturing of orthorhombic rock lithons in the light of the generated fibre stress, when the rock lithon is subjected to a concentrated force. These authors argue that as the concentrated force increases, the stress conditions change due to stress perturbation thus, causing the joints and fracture frequencies to also increase (i.e., a decrease in fracture spacing). This additional fracturing reduces the original size of the rock lithons. That implies that the lithons tend towards a tetragonal or isometric shape by reducing the length distribution of the long axes and by preserving the ones of the short axes (Billi et al., 2003; Fig. 17a through c). In our case example, the fitting boundaries of the reduced size of the rock lithons are preserved in the damage zone of the dolostone fault block (Figs. 2c and 17b, d). These fitting boundaries fade away towards the fault core of the dolostone fault block because of the increased intensity of fracture comminution, and because of significant rotation and crushing of the lithons. Both of these circumstances make the lithons unable to fit in the boundaries between themselves (Fig. 17d).

Geometrically, the values of these lithons aspect ratios below 1 and above 2 represent about 10 and 9% of the total population of the measured lithons respectively. In contrast, 48% of the measured lithon's aspect ratio corresponds to the size range of 1 – 1.6 (Fig. 12b). This suggest that the lithons' aspect ratio are: (i) well clustered, i.e. their values are statistically identical, (ii) independent of the sizes, structural position and the shapes of the lithons (Figs. 12 and 13), and (iii) independent as to whether the lithon is rotated or not especially during the fault core evolution. Billi et al. (2003) argue that the rotation of lithons during the development of the fault core is only possible when the lithon's aspect ratio reaches 1.4. In the case of the lithons documented here, however, the aspect ratio of the rotated and not-rotated (i.e., those that have their boundaries still fitted) is independent of the lithons' dimensions and/or structural position. These observations contrast previous work suggesting a link of the rotation of the lithons to a specific value of its aspect ratio. The shape factor of the lithons reaches an average value of 0.78, implying that majority of the lithons' shapes are equidimensional-to-near rectangular in shape.

Considering a selected scan-line (CF 11c; Fig. 13), the results of the plots reveal that the variations of shape factor are homogenously distributed along the scan-line. This suggests a similar trend to that observed for the aspect ratio. A plot of aspect ratio against shape factor shows a negative gradient, pointing to a decrease in aspect ratio as the shape factor progressively increases (Fig. 13d). These geometrical results give hints on what controls the formation, morphology and rotation of rock lithons. It is important to note that the lithon's formation, morphology and rotation are not entirely controlled by bedding surface but also by the continued triaxial deformation of mutually cross-cutting orthogonal fracture sets.

6.2.2. Topological variability of the dolostone lithons

The topological variability assessed in dolostone fault blocks resulted in a valuable quantitative classification of their 3D connectivity in terms of node and branch topologies (Figs. 14h, i, 15h, i and 16h, i). These variabilities yield important insights into how the fractures within a network evolve, grow, interact and more specifically, connect among themselves. Manzocchi (2002) and Sanderson and Nixon (2015, 2018) have documented how the relative proportion of node and branch topologies vary within a network from single- to multi-connected fracture networks. Single connected networks are dominated by I-node and I-I branch configurations, whereas multi-connected ones are predominantly Y- and X- nodes and I-C, in some cases, C-C branches. Our results reveal that the networks of studied lithons are composed of fewer I-node and I-I branches in comparison to the predominant Y- to X- nodes and I-C to C-C branches (Table 4; Fig. 4). Representing these quantitatively for outcrops CF 9_11, CF 35 and CF 25 respectively, show that: (i) Y (74.7, 56.1, and 49.9%,) to X (19.3, 18.6, and 16.0%) nodes, (ii) I-C (3.8, 16.2, and 23.8%) to C-C (96.2, 82.5 and 73.3%) branches, and (iii) connection-per-branch (C_B; 1.9, 1.8 and 1.7). These representations point to the fact the fracture networks forming lithons are increasingly interacting among themselves, and well-connected. The degree of connectivity maintained a positive relation with the fracture (lithons) intensity (Figs. 14d, e, 15d, e, and 16d, e), which has important implications for the evaluation of the control exerted by dolostone-hosted fault-zones on geofluid migration in the subsurface. In the cases where the matrix permeability is low, fluid follows the pathways of the connected fractures and particularly so at the complex zones where the fracture intensities are high. The pathway provided by these fractures may have contributed in supplying the hydrothermal fluids that overprinted the lithons in the fault zone. Other important areas of application lie in earthquake predictions, ore mineral exploration, et cetera.

6.2.3. The timing of lithons development and Carboneras faulting

The timing between the generation of the lithons and Carboneras faulting is evaluated by means of the bedding orientation distributions and petrography of the dolostone blocks. The stereoplots of the bedding within these dolostone blocks (lithons' and fault block) display remarkable dissimilarities in position (Figs. 17e and 11b), suggest that the blocks are loose, isolated and more or less detached inside the Carboneras fault zone. From the petrographic point of view, our results establish that both the dolostone lithons' and fault blocks have the same history but both units were rotated, dismembered and not spatially linked inside the Carboneras fault zone. Hence, their directions are not consistent in space but only consistent with respect to bedding because the blocks remain internally consistent.

The information regarding the timing and/or age relations between the deformation events that generated the lithons and that of Carboneras faulting are sketchy, the evidence is constrained to the Carboneras fault overprinting relationship on the lithons. The fault overprint initiates the sharp cataclastic zone, in the sense that these blocks are now rotated inside the Carboneras fault zone. A morphological change in shape of the rock lithons ensued, which are largely linked to the cataclastic flow in the Carboneras fault zone. A directional or spatial link of blocks of studied dolostones towards the Carboneras fault is almost impossible, and the formation age of lithons is much older than the Carboneras fault activity. The timing between lithons formation and Carboneras fault zone activity can be explained in only one of two possible scenarios. Either the lithons are related to paleo-faulting (shortly or prior to the Carboneras fault) before being carried into the Carboneras fault, or they are related to the initial stages of deformation of the Carboneras fault.

In conclusion, we document that the dolostone lithons studied here remained brittle over a wide range of conditions. The orthorhombic and thereafter isometric well-connected lithons result from mainly dominant orthogonal sets of discontinuities. Lithons suffered successively localized deformation within the Carboneras fault zone. Lateral changes in lithon size and morphology are observed across the damage zone and fault core within individual dolostone fault block. Prior to undergoing a cataclastic flow, slip localization and rotation takes place and narrow shear zones accommodate displacement.

7. Conclusions

Dolomitized shallow water carbonates were affected by the Neogene Carboneras fault zone. Two main groups of structural features are presently recognised: (1) Features relating to background deformation dominated by low-strain fractures with early embrittlement, and (2) features resulting from the faulting overprint dominated by breccias and cataclasites. Background deformation accommodates fractures in the form of a network of bedding-perpendicular hybrid conjugate veins with a shear component documented by en échelon tension gashes, semi-ductile shear zones, barren fractures and bedding-parallel stylolites. Both, the semi-ductile shear zones and en échelon tension gashes form in conjugate pairs and are largely overprinted by bedding-parallel stylolites.

The Fourier analysis of the spikes of the bedding-parallel stylolites provide evidence for the dolostone burial depths. The results calculated from the reconstructed vertical principal stress ($\sigma 1$) range from 10 to 17.6 MPa and suggest a shallow limit of burial depth in the range of 440 to 820 m.

Orthorhombic lithons generated by one set of joints could be fractured in an orthogonal direction forming the second set of joints, and successively evolve towards a tetragonal or isometric shape. The results of the geometric analysis of the lithons show that the values of the lithon's aspect ratio are statistically identical irrespective of their size, shape and structural position. The analysis of these lithons provides insight into their distributions, and as well their connectivity within the fractured networks.

The topology of the lithons (fracture) networks as characterized by node and branch topologies, indicate that the high fracture intensities and the high connecting node frequencies in structural complex zones (i.e., areas of high fracture interactions) are correlated. In addition, lithons are increasingly interacting among themselves, and are then well connected, based on fracture intersection, cross-cutting and overlapping relationship.

These findings have implications for the understanding of the relationship between the early background deformation, deformation due faulting tectonics, fracture/fault connectivity, brecciation and fluid flow. We considered these data to be relevant to subsurface carbonate reservoirs hosted in fault zones. The quantification of these relationships has the potential to advance predictions of subsurface flow properties.

Acknowledgements

This study was performed in the context of a doctoral research fellowship from Petroleum Technology Development Fund (PTDF) Abuja, Nigeria. The authors thank Quinten Boersma for his assistance on DigiFract software and stylolite data, Jennifer Dikachi-Igbokwe and Charlotte Miller for their time and helpful comments which helped to improve this paper. The authors express their gratitude to the journal editor T. Takeshita, as well as to reviewers D. J. Sanderson, A. Billi, F. Agosta and an anonymous colleague for insightful comments and reviews. Sampling of rocks was not allowed in the Cabo de Gata Natural Parc due to legal restrictions. Given the fact that Carboneras Fault Zone expands beyond the boundaries of the Natural Park, there sampling of all relevant lithologies is possible. Moreover, the authors made use of extensive rock collections at Ruhr-University Bochum from several unpublished PhD projects performed in the 1970's and 1980's in this region.

Data availability

Data used for this study are available upon request to the corresponding author (onyedikachi.igbokwe@rub.de).

References

Agosta, F., Alessandroni, M., Tondi, E., Aydin, A., 2009. Oblique normal faulting along the northern edge of the Majella Anticline, central Italy: Inferences on hydrocarbon migration and accumulation. Journal of Structural Geology. https://doi.org/10.1016/j.jsg.2009.03.012

Agosta, F., Aydin, A., 2006. Architecture and deformation mechanism of a basin-bounding normal fault in Mesozoic platform carbonates, central Italy. Journal of Structural Geology. https://doi.org/10.1016/j.jsg.2006.04.006

Agosta, F., Ruano, P., Rustichelli, A., Tondi, E., Galindo-Zaldívar, J., Sanz de Galdeano, C., 2012. Inner structure and deformation mechanisms of normal faults in conglomerates and carbonate grainstones (Granada Basin, Betic Cordillera, Spain): Inferences on fault permeability. Journal of Structural Geology 45, 4–20. https://doi.org/10.1016/j.jsg.2012.04.003

Alonso-Chaves, F.M., Soto, J.I., Orozco, M., Κίλιας, Α.Α., Τρανός, Μ.Δ., 2004. Tectonic evolution of the Betic Cordillera: an overview. Bulletin of the Geological Society of Greece Vol. XXXVI, 2004 36, 1598–1607.

Aydin, A., 2000. Fractures, faults, and hydrocarbon entrapment, migration and flow. Marine and Petroleum Geology 17, 797–814. https://doi.org/10.1016/S0264-8172(00)00020-9

Beaudoin, N., Koehen, D., Lacomobe, O., Lecouty, A., Billi, A., Aharonov, E., Parlangeau, C., 2016. anticline in the Apennines , Italy. Tectonics 35, 1687–1712.

https://doi.org/10.1002/2016TC004128.Received

Belayneh, M., Cosgrove, J.W., 2010. Hybrid veins from the southern margin of the Bristol Channel Basin, UK. Journal of Structural Geology. https://doi.org/10.1016/j.jsg.2009.11.010

Bertotti, G., de Graaf, S., Bisdom, K., Oskam, B., Vonhof, H.B., H. R. Bezerra, F., J. G. Reijmer, J., L. Cazarin, C., 2017. Fracturing and fluid-flow during post-rift subsidence in carbonates of the Jandaíra Formation, Potiguar Basin, NE Brazil. Basin Research. https://doi.org/10.1111/bre.12246

Billi, A., 2005. Attributes and influence on fluid flow of fractures in foreland carbonates of southern Italy. Journal of Structural Geology 27, 1630–1643. https://doi.org/10.1016/j.jsg.2005.05.001

Billi, A., Salvini, F., Storti, F., 2003. The damage zone-fault core transition in carbonate rocks: Implications for fault growth, structure and permeability. Journal of Structural Geology 25, 1779–1794. https://doi.org/10.1016/S0191-8141(03)00037-3

Bisdom, K., Bertotti, G., Nick, H.M., 2016. The impact of in-situ stress and outcrop-based fracture geometry on hydraulic aperture and upscaled permeability in fractured reservoirs. Tectonophysics. https://doi.org/10.1016/j.tecto.2016.04.006

Caine, J.S., Evans, J.P., Forster, C.B., 1996. Fault zone architecture and permeability structure. Geology 24, 1025–1028. https://doi.org/Doi 10.1130/0091-7613(1996)024<1025:Fzaaps>2.3.Co;2

Chester, F.M., Logan, J.M., 1986. Implications for Mechanical-Properties of Brittle Faults from

Observations of the Punchbowl Fault Zone, California. Pure and Applied Geophysics 124, 79–106. https://doi.org/Doi 10.1007/Bf00875720

Childs, C., Manzocchi, T., Walsh, J.J., Bonson, C.G., Nicol, A., Schöpfer, M.P.J., 2009. A geometric model of fault zone and fault rock thickness variations. Journal of Structural Geology 31, 117–127. https://doi.org/10.1016/j.jsg.2008.08.009

Choi, J.-H., Edwards, P., Ko, K., Kim, Y.-S., 2016. Definition and classification of fault damage zones: A review and a new methodological approach. Earth-Science Reviews 152, 70–87. https://doi.org/https://doi.org/10.1016/j.earscirev.2015.11.006

De Larouzière, F.D., Bolze, J., Bordet, P., Hernandez, J., Montenat, C., d'Estevou, P.O., 1988. The Betic segment of the lithospheric Trans-Alboran shear zone during the late Miocene. Tectonophysics 152, 41–52.

Dimmen, V., Rotevatn, A., Peacock, D.C.P., Nixon, C.W., Naeland, K., 2017. Quantifying structural controls on fluid flow: Insights from carbonate-hosted fault damage zones on the Maltese Islands. Journal of Structural Geology 101, 43–57. https://doi.org/10.1016/j.jsg.2017.05.012

Doblas, M., Mahecha, V., Hoyos, M., 1997. Slickenside and fault surface kinematic indicators on active normal faults of the Alpine Betic cordilleras, Granada, southern Spain. Journal of Structural Geology 19, 159–170. https://doi.org/Doi 10.1016/S0191-8141(96)00086-7

Duffy, O.B., Nixon, C.W., Bell, R.E., Jackson, C.A.L., Gawthorpe, R.L., Sanderson, D.J., Whipp, P.S., 2017. The topology of evolving rift fault networks: Single-phase vs multi-phase rifts. Journal of Structural Geology 96, 192–202. https://doi.org/10.1016/j.jsg.2017.02.001

Ebner, M., Koehn, D., Toussaint, R., Renard, F., 2009a. The influence of rock heterogeneity on the scaling properties of simulated and natural stylolites. Journal of Structural Geology. https://doi.org/10.1016/j.jsg.2008.10.004

Ebner, M., Koehn, D., Toussaint, R., Renard, F., Schmittbuhl, J., 2009b. Stress sensitivity of stylolite morphology. Earth and Planetary Science Letters 277, 394–398. https://doi.org/10.1016/j.epsl.2008.11.001

Faulkner, D.R., Lewis, A.C., Rutter, E.H., 2003. On the internal structure and mechanics of large strike-slip fault zones: field observations of the Carboneras fault in southeastern Spain. Tectonophysics 367, 235–251. https://doi.org/10.1016/s0040-1951(03)00134-3

Faulkner, D.R., Mitchell, T.M., Rutter, E.H., Cembrano, J., 2008. On the structure and mechanical properties of large strike-slip faults. Geological Society, London, Special Publications 299, 139–150. https://doi.org/10.1144/sp299.9

Fletcher, R.C., Pollard, D.D., 1981. Anticrack model for pressure solution surfaces. Geology 9, 419–424. https://doi.org/10.1130/0091-7613(1981)9<419:AMFPSS>2.0.CO;2

Frizon, D. de L., Andrieux, J., Guezou, J.-C., 1991. Cinématique des chevauchements Néogènes dans l’arc bético-Rifains, discussion sur les modèles géodynamiques. https://doi.org/10.2113/gssgfbull.162.4.611

Igbokwe, O.A., Mueller, M., Abah, O., Bertotti, G., Immenhauser, A., 2018. Morphological changes of carbonate deformed clasts in a neogene fault zone. 3rd EAGE Workshop on Naturally Fractured Reservoirs. European Association of Geoscientists and Engineers, EAGE. https://doi.org/10.3997/2214-4609.201800040

Jourde, H., Flodin, E.A., Aydin, A., Durlofsky, L.J., Wen, X.H., 2002. Computing permeability of fault zones in eolian sandstone from outcrop measurements. AAPG Bulletin 86, 1187–1200. https://doi.org/10.1306/61eedc4c-173e-11d7-8645000102c1865d

Kampschuur, W., Rondeel, H.E., 1975. The origin of the Betic Orogen, southern Spain. Tectonophysics 27, 39–56.

Keller, J.V.A., Hall, S.H., Dart, C.J., Mcclay, K.R., 1995. The Geometry and Evolution of a Transpressional Strike-Slip System - the Carboneras Fault, Se Spain. Journal of the Geological Society 152, 339–351. https://doi.org/DOI 10.1144/gsjgs.152.2.0339

Keller, J.V.A., Hall, S.H., McClay, K.R., 1997. Shear fracture pattern and microstructural evolution in transpressional fault zones from field and laboratory studies. Journal of Structural Geology 19, 1173–1187. https://doi.org/10.1016/S0191-8141(97)00042-4

Kim, Y.S., Peacock, D.C.P., Sanderson, D.J., 2004. Fault damage zones. Journal of Structural Geology. https://doi.org/10.1016/j.jsg.2003.08.002

Kirschner, D.L., Teyssier, C., 1994. Orthorhombically arranged vein arrays. Journal of Structural Geology 16, 1129–1138. https://doi.org/10.1016/0191-8141(94)90057-4

Korneva, I., Tondi, E., Agosta, F., Rustichelli, A., Spina, V., Bitonte, R., Di Cuia, R., 2014. Structural properties of fractured and faulted Cretaceous platform carbonates, Murge Plateau (southern Italy). Marine and Petroleum Geology. https://doi.org/10.1016/j.marpetgeo.2014.05.004

Lamarche, J., Lavenu, A.P.C., Gauthier, B.D.M., Guglielmi, Y., Jayet, O., 2012. Relationships between fracture patterns, geodynamics and mechanical stratigraphy in Carbonates (South-

East Basin, France). Tectonophysics 581, 231–245. https://doi.org/10.1016/j.tecto.2012.06.042

Larsen, B., Gudmundsson, A., Grunnaleite, I., Sælen, G., Talbot, M.R., Buckley, S.J., 2010. Effects of sedimentary interfaces on fracture pattern, linkage, and cluster formation in peritidal carbonate rocks. Marine and Petroleum Geology. https://doi.org/10.1016/j.marpetgeo.2010.03.011

Lavenu, A.P.C., Lamarche, J., Salardon, R., Gallois, A., Marié, L., Gauthier, B.D.M., 2014. Relating background fractures to diagenesis and rock physical properties in a platform-slope transect. Example of the Maiella Mountain (central Italy). Marine and Petroleum Geology. https://doi.org/10.1016/j.marpetgeo.2013.11.012

Manzocchi, T., 2002. The connectivity of two-dimensional networks of spatially correlated fractures. Water Resources Research. https://doi.org/10.1029/2000wr000180

Morales, J., Serano, I., Jabaloy, A., Galindo-Zaldívar, J., Zhao, D., Torcal, F., Vidal, F., González-Lodeiro, F., 1999. Active continental subduction beneath the Betic Cordillera and the Alboran Sea. Geology 27, 735–738. https://doi.org/10.1130/0091-7613(1999)027<0735:ACSBTB>2.3.CO;2

Morley, C.K., Nixon, C.W., 2016. Topological characteristics of simple and complex normal fault networks. Journal of Structural Geology 84, 68–84. https://doi.org/10.1016/j.jsg.2016.01.005

Mort, K., Woodcock, N.H., 2008. Quantifying fault breccia geometry: Dent Fault, NW England. Journal of Structural Geology 30, 701–709. https://doi.org/10.1016/j.jsg.2008.02.005

Mueller, M., Igbokwe, O.A., Walter, B., Pederson, C.L., Riechelmann, S., Richter, D.K., Albert, R., Gerdes, A., Buhl, D., Neuser, R.D., Bertotti, G., Immenhauser, A., 2020. Testing the preservation potential of early diagenetic dolomites as geochemical archives. Sedimentology 67 (2), 849-881. https://doi.org/10.1111/sed.12664

Nixon, C.W., Sanderson, D.J., Dee, S.L., Bull, J.M., Humphreys, R.J., Swanson, M.H., 2014. Fault interactions and reactivation within a normal-fault network at Milne Point, Alaska. AAPG Bulletin 98, 2081–2107. https://doi.org/10.1306/04301413177

Nyberg, B., Nixon, C.W., Sanderson, D.J., 2018. NetworkGT: A GIS tool for geometric and topological analysis of two-dimensional fracture networks. Geosphere. https://doi.org/10.1130/GES01595.1

Oertel, G., 1965. The mechanism of faulting in clay experiments. Tectonophysics 2, 343–393. https://doi.org/10.1016/0040-1951(65)90032-6

Peacock, D C P, Nixon, C.W., Rotevatn, A., Sanderson, D.J., Zuluaga, L.F., 2016. Glossary of fault and other fracture networks. Journal of Structural Geology 92, 12–29. https://doi.org/10.1016/j.jsg.2016.09.008

Pollard, D.D., Aydin, A., 1988. Progress in understanding jointing over the past century. Special Paper of the Geological Society of America. 313–336. https://doi.org/10.1130/SPE253-p313

Pollard, D.D., Fletcher, R.C., 2006. Fundamentals of structural geology. Choice Reviews Online 43, 43-5304-43–5304. https://doi.org/10.5860/CHOICE.43-5304

Ramsay, J.G., 1980. Shear zone geometry: A review. Journal of Structural Geology 2, 83–99. https://doi.org/10.1016/0191-8141(80)90038-3

Reches, Z., 1983. Faulting of rocks in three-dimensional strain fields II. Theoretical analysis. Tectonophysics 95, 133–156. https://doi.org/10.1016/0040-1951(83)90264-0

Reches, Z., Dieterich, J.H., 1983. Faulting of rocks in three-dimensional strain fields I. Failure of rocks in polyaxial, servo-control experiments. Tectonophysics 95, 111–132. https://doi.org/10.1016/0040-1951(83)90263-9

Renard, F., Schmittbuhl, J., Gratier, J., Meakin, P., Merino, E., 2004. Three-dimensional roughness of stylolites in limestones. Journal of Geophysical Research 109. https://doi.org/10.1029/2003jb002555

Rutter, E.H., Burgess, R., Faulkner, D.R., 2014. Constraints on the movement history of the Carboneras Fault Zone (SE Spain) from stratigraphy and 40Ar–39Ar dating of Neogene volcanic rocks. Geological Society, London, Special Publications 394, 79–99. https://doi.org/10.1144/sp394.5

Rutter, E.H., Faulkner, D.R., Burgess, R., 2012. Structure and geological history of the Carboneras Fault Zone, SE Spain: Part of a stretching transform fault system. Journal of Structural Geology 45, 68–84. https://doi.org/10.1016/j.jsg.2012.08.009

Sanderson, D.J., Nixon, C.W., 2018. Topology, connectivity and percolation in fracture networks. Journal of Structural Geology. https://doi.org/10.1016/j.jsg.2018.07.011

Sanderson, D.J., Nixon, C.W., 2015. The use of topology in fracture network characterization. Journal of Structural Geology 72, 55–66. https://doi.org/10.1016/j.jsg.2015.01.005

Schmittbuhl, J., Renard, F., Gratier, J.P., Toussaint, R., 2004. Roughness of stylolites: Implications of 3D high resolution topography measurements. Physical Review Letters.

https://doi.org/10.1103/PhysRevLett.93.238501

Segall, P., Pollard, D.D., 1983. Nucleation and Growth of Strike Slip Faults in Granite. Journal of Geophysical Research 88, 555–568. https://doi.org/DOI 10.1029/JB088iB01p00555

Shipton, Z.K., Cowie, P.A., 2003. A conceptual model for the origin of fault damage zone structures in high-porosity sandstone (vol 25, pg 333, 2003). Journal of Structural Geology 25, 1343–1345. https://doi.org/10.1016/S0191-8141(03)00060-9

Sibson, R.H., 2000. Fluid involvement in normal faulting. Journal of Geodynamics 29, 469–499. https://doi.org/Doi 10.1016/S0264-3707(99)00042-3

Sibson, R.H., 1977. Fault rocks and fault mechanisms. Journal of the Geological Society 133, 191–213. https://doi.org/10.1144/gsjgs.133.3.0191

Srivastava, D.C., Engelder, T., 1990. Crack-propagation sequence and pore-fluid conditions during fault-bend folding in the Appalachian Valley and Ridge, central Pennsylvania. GSA Bulletin 102, 116–128. https://doi.org/10.1130/0016-7606(1990)102<0116:cpsapf>2.3.co;2

Tondi, E., 2007. Nucleation, development and petrophysical properties of faults in carbonate grainstones: Evidence from the San Vito Lo Capo peninsula (Sicily, Italy). Journal of Structural Geology 29, 614–628. https://doi.org/10.1016/j.jsg.2006.11.006

Turcotte, D., Schubert, G., 2002. Geodynamics, Second Edition, Eos, Transactions American Geophysical Union. https://doi.org/10.1029/2003eo180009

Visser, R.L.., Platt, J.P., van der Wal, D., 1995. the Alboran Domain: A lithospheric. Tectonics 14, 786–803. https://doi.org/10.1029/95TC00086

Figure captions

Fig. 1. Simplified geological map of the Carboneras Fault. **(A)** Regional map displaying the location of the Carboneras fault in the tectonic framework of S.E. Spain. SLF = Sierra de Los Filabres, SA = Sierra Alhamilla, SC = Sierra Cabrera, NB = Nijar Basin, SB = Sorbas Basin, VB = Vera Basin (after Faulkner et al. 2008). **(B)** Tectonic map of the Carboneras Fault Zone. The map displays the Neogene-Quaternary deposits of the Carboneras Nijar and Vera basins locating the main Paleozoic-Mesozoic basement culminations and main fault zones in the area (Modified after Keller et al., 1997).

Fig. 2. (A) The Google hybrid satellite image of the Carboneras Fault Zone, including the locations of different analysed outcrops and sampling points. **(B)** Block diagram of lithon's block showing lithons and preserved features such as bedding planes, stylolites, veins etc. **(C)** Block diagram of fault block indicating damage zone and fault core with both abrupt and gradual transition (often characterized by a main fault surface). Red box is enlarged in figure 17d.

Fig. 3. Photographs of outcrop-scale fault-related deformation in the Carboneras fault zone. **(A)** A view to the NE with 100m-size blocks of faulted strata inside the fault zone. Note the Neogene Azagador Formation overlying the Carboneras fault gouge and dolostones. **(B)** Homogeneous distribution of strain within the phyllosilicate-rich gouge layer developed within the graphitic mica schist. See hammer (28 x 19 cm) for scale. **(C** through **E)** Massive to poorly layered dolostone fault blocks, showing complex variations of lithons size and a moderate-to-sharp transition between damaged zone, breccia and gouge. **(F)** Interlayered breccias and cataclasite, showing complex variations in lithons dimension and transitions between the dolostone, damaged zone and

fault core (breccia and gouge). **(G)** Conceptual diagram showing by what method lithons dimension (aspect ratio, shape factor, width, aperture and height) were measured.

Fig. 4. (A) Fracture trace (A – B), with accompanying intersecting fractures (dashed), displaying arrangement of nodes and branches: I-nodes (green circles); Y-nodes (red triangles); X-nodes (blue diamonds). **(B)** Branch classification plot, showing proportions of different branch types with number 0 – 2 indicating connections per branch (C_B). The curve shows results from the three studied dolostone fault blocks. **(C)** Values of number of connections per branch (C_B), showing proportion of different nodes, together with corresponding node proportion for networks of Carboneras dolostone fault blocks. Modified after Sanderson and Nixon (2015).

Fig. 5. (A) Typical outcrop features of dolostone lithons' block within the Carboneras fault zone. Note alternation of dark and light-coloured bands related to fining-upward cycles. **(B)** Plane polarized light image showing finely laminated early diagenetic shoalwater dolostones including stylolites overprint. **(C)** The cross-cutting relation of a bedding-perpendicular dolomitic vein and a bedding-parallel stylolite (blue arrow), indicating that fracturing and vein infill predated burial stylolite formation. Also, a much younger vein (yellow arrow) displacing and/or overprinting the bedding-parallel stylolites. Note image was taken under plane polarized light. **(D** and **E)** A gradual transition with a nice close-up within the dolomite showing alternation between the fine-grained dolomite generation (Dol.1) and coarse-grained dolomite generation (Dol. 2; Images were taken under crossed polarized light). **(F** and **G)** Show plane polarized light and the corresponding cathodoluminescence images of the diagenetic dolostones with a late bedding-perpendicular vein

overprinting bedding parallel stylolites. (**H**) Dolomite filled vugs and zebra fabrics with characteristics bedding parallel stylolites (blue arrows).

Fig. 6. (A through **C)** Microscale observation of component size of breccias and cataclasites distribution. **(D** and **E)** Plane polarized light images of both breccia and cataclasite. **(F** and **G)** Crossed polarized light images of cataclasite showing spheroidal/blocky calcite overgrowth entirely enclosing the clasts in F and G (enlargement of F). Samples were taken from outcrop CF 1.

Fig. 7. (A through **C)** Photograph of detailed background structural features within the dolostone lithons' blocks showing both semi-ductile shear zones (red dashed and dotted lines) and conjugate hybrid veins. The veins (yellow short-lines) consist of left- and right-stepping *en échelon* veins with acute bisector of a 25^{o} **(A),** 55^{o} **(B)**, and 15^{o} **(C)**. The stylolites in (A through C) overprint the hybrid veins. **(i)** Left-stepping en échelon veins indicating a dextral sense of displacement, **(ii)** right-stepping en échelon veins indicating sinistral sense of movement.

Fig. 8. Photographs of dolostone lithons' block prior to faulting overprint showing deformation caused by *en échelon* veins, semi-ductile shear zones, bedding-perpendicular veins and stylolites with their cross-cutting relationships. **(A)** Displays the shear zones, the conjugate pattern of the *en échelon* veins and bisecting bedding-perpendicular elongate veins, all being overprinted by bedding parallel stylolites. **(B)** Stereoplot of the geometric elements shown in A. **(C)** Stereoplot of geometric elements position of shear fractures and veins once bedding is rotated back to horizontal. **(D)** Shows veins arrested against the bedding parallel stylolites and joint tip lying within the

laminated dolostone block. **(E)** Enlargement of figure 7c, showing overprinting relations between *en échelon* (pull-aparts), bedding-perpendicular veins and stylolites. Note the clear finning-upward cycles of alternating dark and light gray dolomite bands. **(F)** Zebra fabric overprinted by *en échelon* veins and bedding-parallel stylolites.

Fig. 9. Small pavement (CF18) used in characterising the geometry of the bedding-perpendicular veins not entirely reactivated during exhumation. **(A)** Orthorectified image of the pavement (CF18) showing wall-matching and reactivated veins. **(B)** Digitized vein networks with vein sets; set 1 (in red), set 2 (in blue) and set 3 (in gray). **(C)** Rose diagrams of vein strikes. **(D)** Length distribution of veins in CF18. See pencil in figures (A and B; length 12 cm) for scale.

Fig. 10. Bedding-parallel stylolites (from outcrop CF 3) in the Carboneras Fault Zone. **(A)** Plane section of a sample cut perpendicular to the mean stylolitic plane with spike-like structures oriented parallel to the principal stress direction. **(B)** 1D roughness of stylolites shown in A after overhangs and linear trend have been removed. **(C)** Binned data of the Fourier power spectrum of B with a well-defined crossover length scale. **(D)** Fourier analysis of the roughness of stylolites. Fourier power spectrum is plotted against the inverse of the wavelength of roughness.

Fig. 11. (A) Line drawing and structural sketch from a photography of a selected dolostone fault block. Within the fault block, a N137^0 – striking boundary fault delineate the damage zone and the fault core. **(B)** Histogram of fracture dips indicating a largely sub-vertical to vertical fractures (adapted from Igbokwe et al., 2018). **(C)** Stereoplot of the structural elements that are present in A. **(D** through **I)** Show fracture spacing along selected 6 scan lines measured in the dolostone

blocks. Red color in D and E highlight filled fractures. The number of measured spacing is approximately N = 450 and the analysed outcrops are shown in figure 2a.

Fig. 12. Lithon's geometrical analysis and/or frequency histograms of lithon's aspect ratio. **(A)** Relation between the lithon's long side and short side. **(B)** Overall lithons' aspect ratio. **(C)** Aspect ratio of selected scan-lines in the dolostone blocks. **(D)** Histogram of L (long side of lithon sections) population, and **(E)** Histogram of l (short side of lithon sections) population as sampled at the selected scan-lines of the dolostones blocks. See figure 2a for the location of different analysed outcrops.

Fig. 13. Lithon's shape factor, diameter, and aspect ratio analysis for a selected transect (Scan-line CF 11c). **(A)** Frequency histogram for of lithon's shape factor. **(B)** Distribution of lithons diameter-showing a downward decrease across the scan-line. **(C)** Distribution of aspect ratio within the transect. **(D)** Relation between the lithon's shape factor and aspect ratio

Fig. 14. The network of open (barren) fractures and topological parameters of the Carboneras dolostones fault block (CF 9_11). **(A)** High-resolution 2D outcrop orthorectified photograph. **(B)** Map of the digitized barren fracture patterns in two sets; set 1 (red) and set 2 (blue). **(C)** Topology of fracture network classified into nodes and branches. **(D)** Map showing the fracture abundance measure "fracture intensity". **(E)** Map showing topological parameter "connecting node frequency". **(F)** Rose diagram of plotted fractures in different sets. **(G)** Distribution analysis of fracture lengths using a series of cumulative frequency plots and a table of statistics for the entire fracture network. **(H)** Branch classification plotted on an I-I, C-I, and C-C ternary diagram. **(I)**

Node classification plotted on an I, Y, and X ternary diagram. The lines indicate thresholds of number of connections per branch ranging from 0 to 2.

Fig. 15. The network of open (barren) fractures and topological parameters of the Carboneras dolostone fault block (CF 35). **(A)** High-resolution 2D outcrop orthorectified photograph. **(B)** Map of the digitized barren fracture patterns; set 1 (in red), set 2 (in blue), set 3 (in gray). **(C)** Topology of fracture network classified into nodes and branches. **(D)** Map showing the fracture abundance measure "fracture intensity". **(E)** Map showing topological parameter "connecting node frequency". **(F)** Rose diagram of plotted fractures in different sets. **(G)** Distribution analysis of fracture lengths using a series of cumulative frequency plots and a table of statistics for the entire fracture network. **(H)** Branch classification plotted on an I-I, C-I, and C-C ternary diagram. **(I)** Node classification plotted on an I, Y, and X ternary diagram. The lines indicate thresholds of number of connections per branch ranging from 0 to 2.

Fig. 16. The network of open (barren) fractures and topological parameters of the Carboneras dolostone fault block (CF 25). **(A)** High-resolution 2D outcrop orthorectified photograph. **(B)** Map of the digitized barren fracture patterns. **(C)** Topology of fracture network classified into nodes and branches. **(D)** Map showing the fracture abundance measure "fracture intensity". **(E)** Map showing topological parameter "connecting node frequency". **(F)** Rose diagram of plotted fractures in different sets. **(G)** Distribution analysis of fracture lengths using a series of cumulative frequency plots and a table of statistics for the entire fracture network. **(H)** Branch classification plotted on an I-I, I-C, and C-C ternary diagram. **(I)** Node classification plotted on an I, Y, and X

ternary diagram. The lines indicate thresholds of number of connections per branch ranging from 0 to 2.

Fig. 17. Schematic illustration of progressive fracturing of orthorhombic lithons into isometric lithons (after Billi et al., 2003). **(A)** Orthorhombic lithon is generated by the intersection of the dominant fracture with bedding and/or joints. **(B)** Expected joints cut across the dominant orthorhombic lithons, creating lithons with a vertical long axis that is nearly tetragonal. **(C)** A second set of joints cut the long axis of the tetragonal lithons to create an isometric lithon. **(D)** Enlargement of figure 2c, showing schematic drawing of a dolostone fault block with both lithons fitting the boundaries and those that do not fit the boundaries. **(E)** Bedding orientations of a few selected dolostone lithons' and fault blocks from both NE and NW reach of the east west segment of Carboneras fault zone. The orientations show that both blocks have been significantly rotated in the fault zone.

Appendix A

A.1. Material and methods

A.1.1. Stylolite analysis as a proxy for compressive stress and burial depth

A set of five bedding-parallel stylolites were collected within the sample locations marked as CF 2, CF 3 and CF 6 in Figure 2a. The samples were cut normal to the main stylolitic plane and polished. Each slab was scanned with an EPSO Perfection V550 photo scanner and the traces of the stylolites were digitized in GIS environment (QGIS 3.2.1). The Fourier Power Spectra P(k) as a function of the wave-number k [1/length scale (mm^{-1})] for each stylolite pattern was calculated and plotted to determine the cross-over wavelength between the two self-affine regimes corresponding to the elastic energy dominated regime at large-scale and surface energy dominated regime at small-scale. The cross-over length (*Lc*) gives a value for the causative stress on the stylolite interface and is linked in the equation below.

$Lc = \frac{\gamma E}{\beta \sigma_{mean} \sigma_{differential}}$, ………………………………………(2) where γ is the surface free energy, E the Young modulus, β a function of the Poisson ratio ($\beta = \frac{2v(1-2v)}{\pi}$). Assuming that gravity is the only stress present and the strain is uniaxial (i.e. zero horizontal displacements), then the horizontal components is a function of the vertical stress component σ_z. Eq. (2) is modified after Ebner et al. (2009b) to $Lc = \frac{3\gamma E}{\beta\left(a(\sigma z)^{\frac{1}{2}} + b\sigma z - C\right)}$………………………..(3)

Expressing mean and differential stress in σ_z using a quadratic equation give; $a = 1 + \left(\frac{v}{1-v}\right) - 2\left(\frac{v}{1-v}\right)^2$; $b = \sigma_{tect} - 3\sigma_{tect}\left(\frac{v}{1-v}\right)^2 - \sigma_{tect}\left(\frac{v}{1-v}\right)$; $c = \left(\frac{v}{1-v}\right)^2 \sigma_{tect}^2 + \left(\frac{v}{1-v}\right)\sigma_{tect}^2$

The vertical stress $\sigma_z = \rho g z$, where ρ is density, g is acceleration due to gravity and z is depth. Sub-vertical tectonic stylolites were not considered, thus $\sigma_{tect} = 0$; c = 0 and b = 0; then

$$\sigma_z = +/- \left(\frac{3\gamma E}{a\beta Lc}\right)^{1/2} \text{ ……………………… (4)}$$

To extract values of the vertical stresses and the corresponding depths of stylolite formation, parameters shown in Table 1 were adopted. Values obtained from different samples lead to directly comparable results, a feature that is considered promising.

A.2. Results

A.2.1. Microscale structures and microscopic observations of the overprinted dolostone fault core.

The fault rocks show striking contrast in component size of cataclastic distribution, and intact polycrystalline fragments of variable sizes (with no damage at the grain scale) contained within a matrix of cata-to ultra-cataclasite. The transitions between the component sizes of the cataclasite are largely sharp. Elsewhere, the fine-grained component of the cataclasites gradually pass onto coarse-grained components (Fig. 6a – c). The coarse-grained fragments are surrounded by small to very-small clasts of dolomite matrix (clast-supported), while the fine-grained lithons are dispersed within a very-fined-grained matrix of dolomites (matrix-supported). The matrix of both clasts contains a minor amount of calcite cement resulting from late burial or meteoric diagenesis (Fig. 6a, f and g).

In the clast-supported samples from the breccia zone, the calcite veins precipitated around the clast, and stylolites constrained within each individual clast are predominant. The overall grain-sizes are partly sorted. A more distinctive feature of the clast-supported dolostone breccias is that of the spheroidal calcite overgrowth (Fig. 6f and g). Each clast is entirely enclosed by a spheroidal/blocky calcite overgrowth such that the clasts are not in contact with their neighbours. Spheroidal calcite overgrowths, along with cements between the spheroids, typically form between 5 and 10 vol. percent of the dolostone breccias. The calcite spheroids are moderately to weakly cemented.

In the matrix supported samples, coarse grained clasts are broken and embedded in a fine-to-a very fine matrix of crushed dolomites. In some cases, broken clasts are cemented by large dolomite crystals to produce a compact rock which underwent subsequent localized deformation. But besides, there is a second brecciation within the fine matrix (Fig. 6e). No stylolites or other evidence of dissolution features were observed within the matrix.

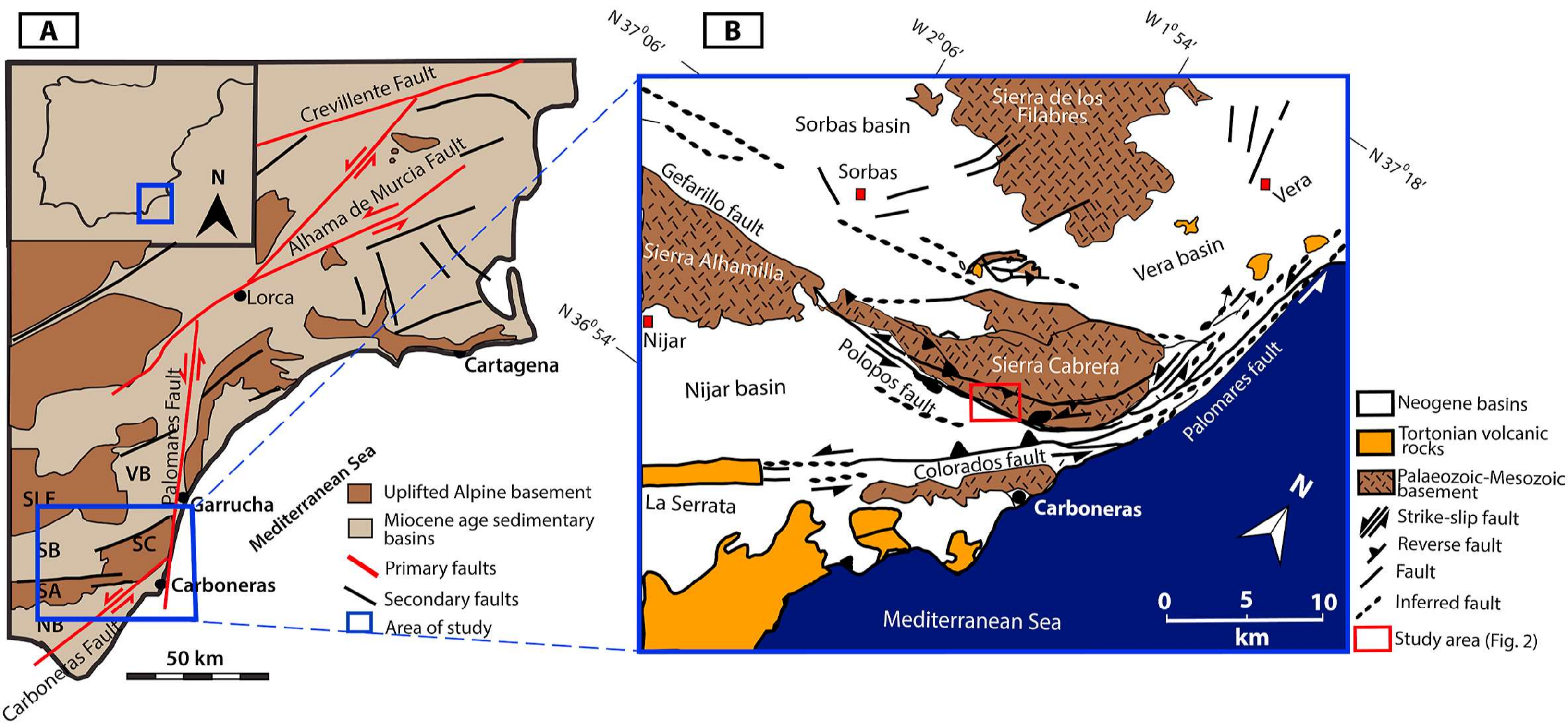

A
Crevillente Fault
Alhama de Murcia Fault
N
Lorca
Cartagena
Palomares Fault
VB
SLF
SB
SA
NB
SC
Garrucha
Carboneras
Carboneras Fault
Mediterranean Sea
50 km
Uplifted Alpine basement
Miocene age sedimentary basins
Primary faults
Secondary faults
Area of study
B
N 37°06'
W 2°06'
W 1°54'
N 37°18'
N 36°54'
Sorbas basin
Sierra de los Filabres
Sorbas
Vera
Gefarillo fault
Sierra Alhamilla
Vera basin
Nijar
Nijar basin
Polopos fault
Sierra Cabrera
Palomares fault
Colorados fault
La Serrata
Carboneras
Mediterranean Sea
0 5 10
km
Neogene basins
Tortonian volcanic rocks
Palaeozoic-Mesozoic basement
Strike-slip fault
Reverse fault
Fault
Inferred fault
Study area (Fig. 2)

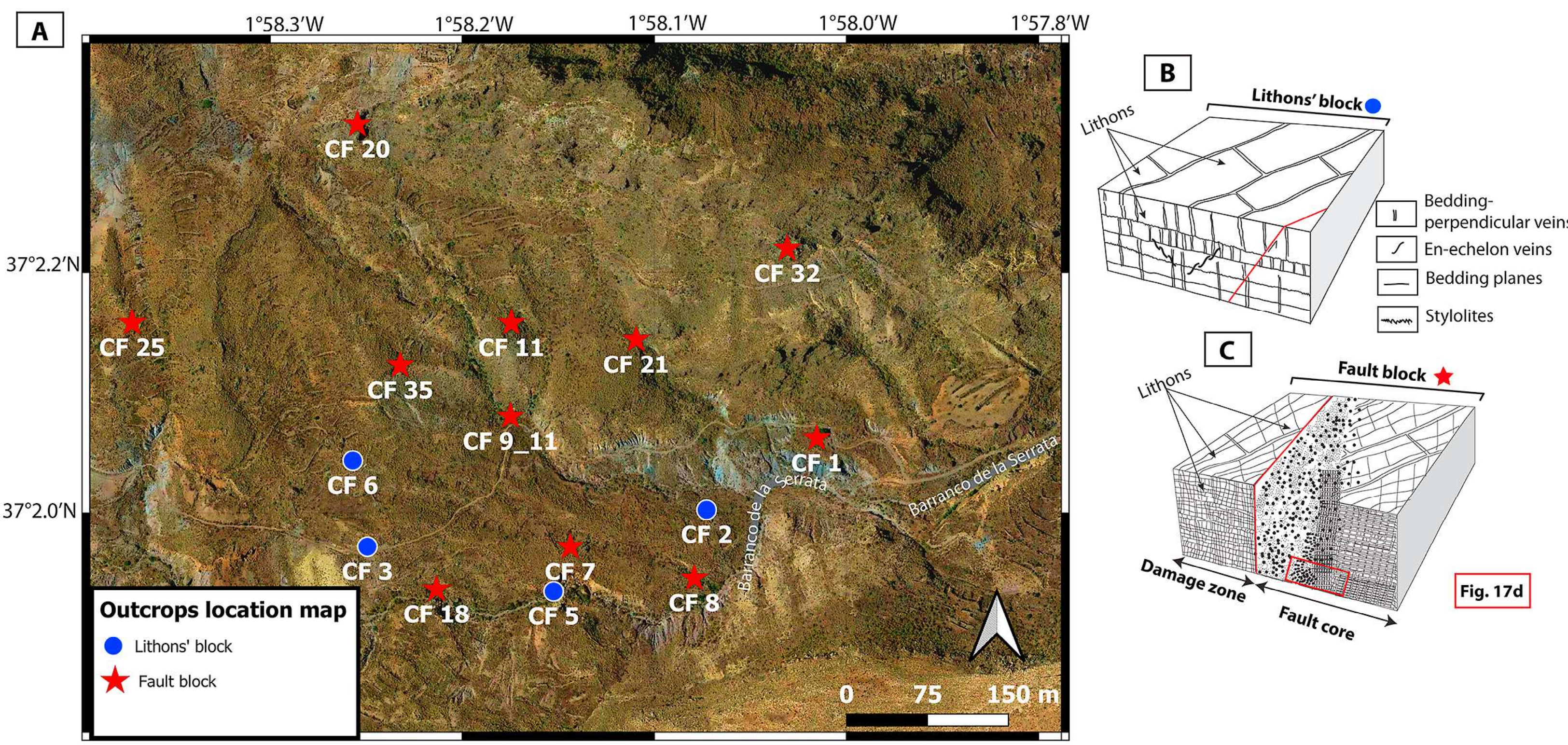
A
1°58.3'W
1°58.2'W
1°58.1'W
1°58.0'W
1°57.8'W
37°2.2'N
37°2.0'N
CF 20
CF 32
CF 25
CF 11
CF 21
CF 35
CF 9_11
CF 1
CF 6
CF 2
CF 3
CF 7
CF 18
CF 5
CF 8
Barranco de la Serrata
Barranco de la Serrata
Outcrops location map
Lithons' block
Fault block
0
75
150 m
B
Lithons' block
Lithons
Bedding-perpendicular veins
En-echelon veins
Bedding planes
Stylolites
C
Fault block
Lithons
Damage zone
Fault core
Fig. 17d

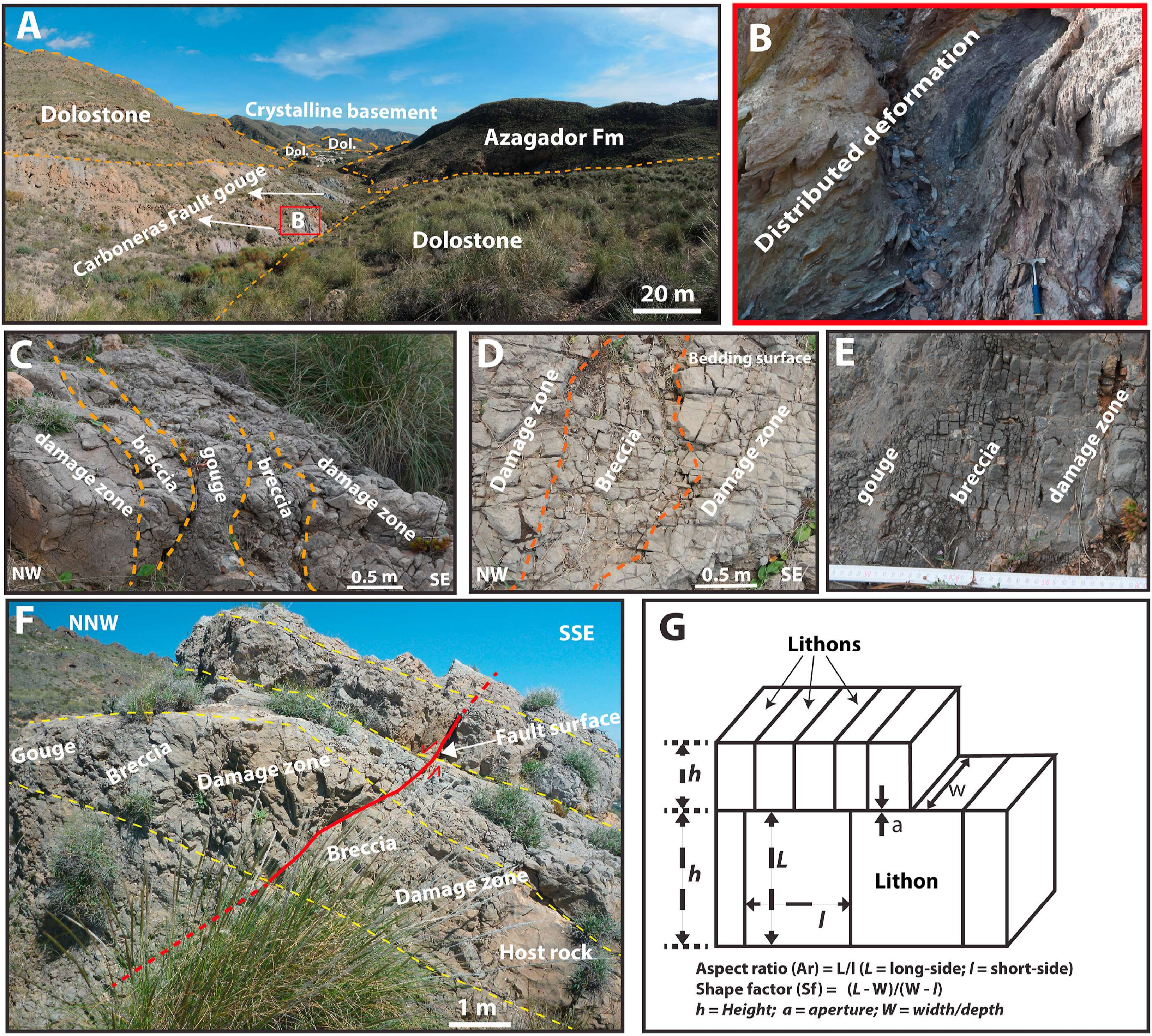
A
Dolostone
Crystalline basement
Dol.
Dol.
Azagador Fm
Carboneras Fault gouge
B
Dolostone
20 m
B
Distributed deformation
C
damage zone
breccia
gouge
breccia
damage zone
NW
0.5 m
SE
D
Bedding surface
Damage zone
Breccia
Damage zone
NW
0.5 m
SE
E
gouge
breccia
damage zone
F
NNW
SSE
Fault surface
Gouge
Breccia
Damage zone
Breccia
Damage zone
Host rock
1 m
G
Lithons
h
h
w
a
L
l
Lithon
Aspect ratio (Ar) = L/l (L = long-side; l = short-side)
Shape factor (Sf) = (L - W)/(W - l)
h = Height; a = aperture; W = width/depth

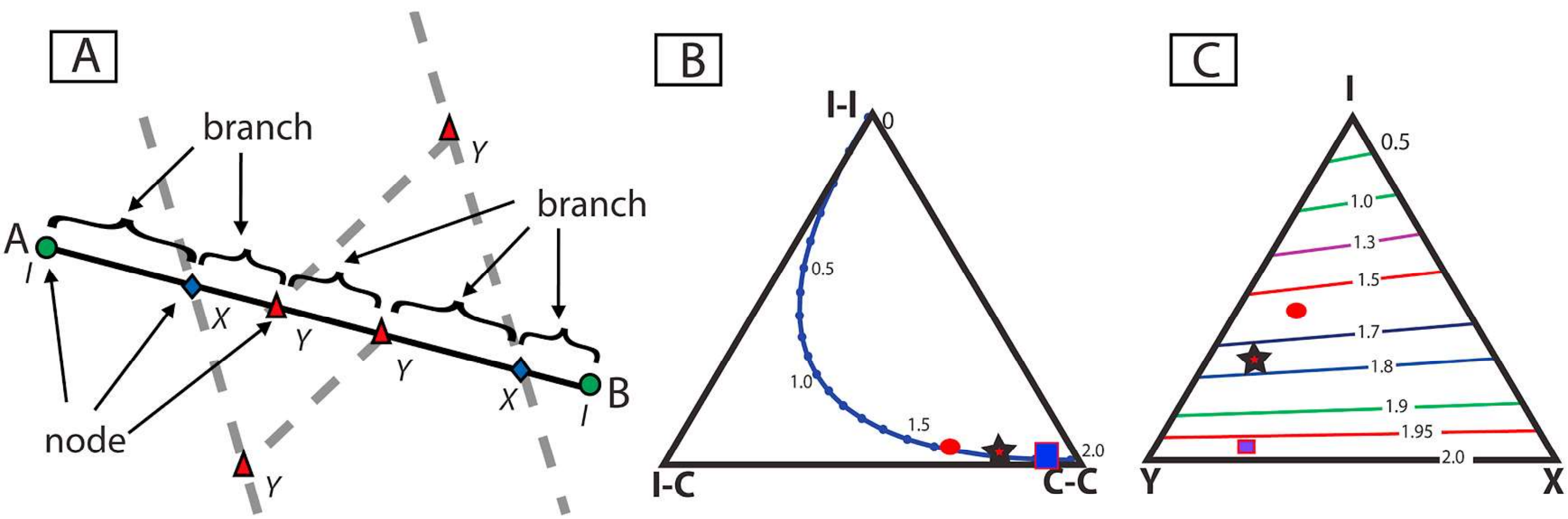

A
branch
branch
A
I
X
Y
Y
Y
Y
X
B
I
node
B
I-I
0
0.5
1.0
1.5
2.0
I-C
C-C
C
I
0.5
1.0
1.3
1.5
1.7
1.8
1.9
1.95
2.0
Y
X

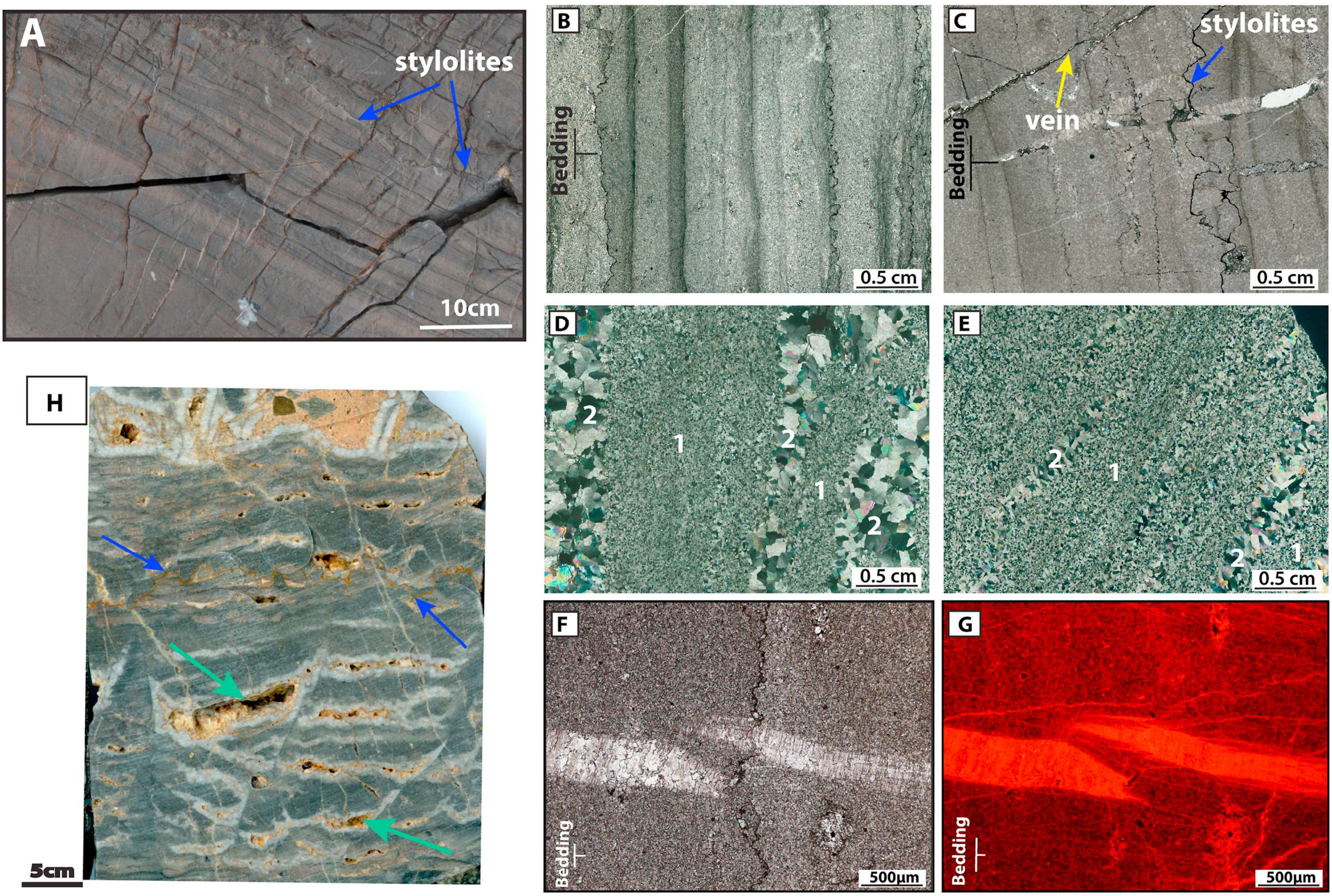

A
stylolites
10cm
B
Bedding
0.5 cm
C
stylolites
vein
Bedding
0.5 cm
D
2
1
2
1
2
0.5 cm
E
2
1
2
1
0.5 cm
F
Bedding
500µm
G
Bedding
500µm
H
5cm

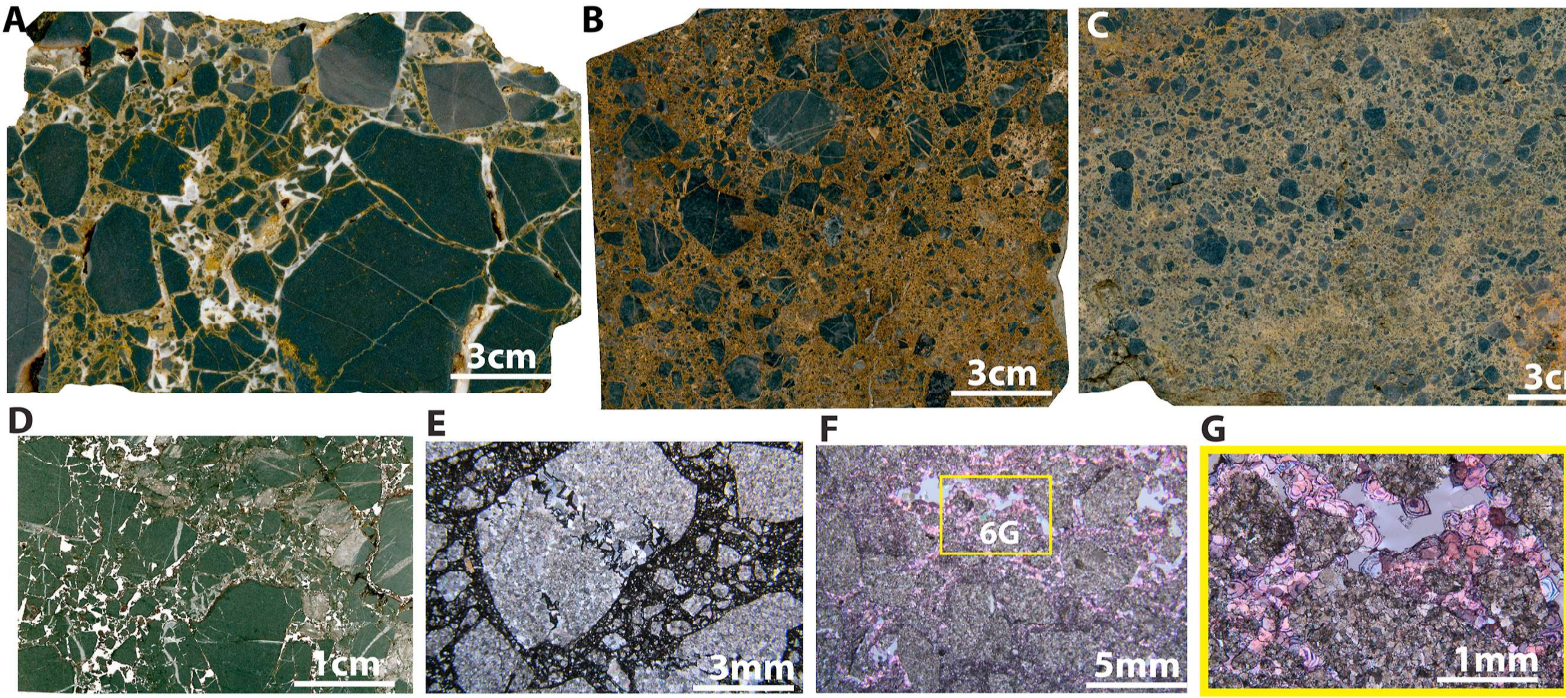

A
3cm
B
3cm
C
3cm
D
1cm
E
3mm
F
6G
5mm
G
1mm

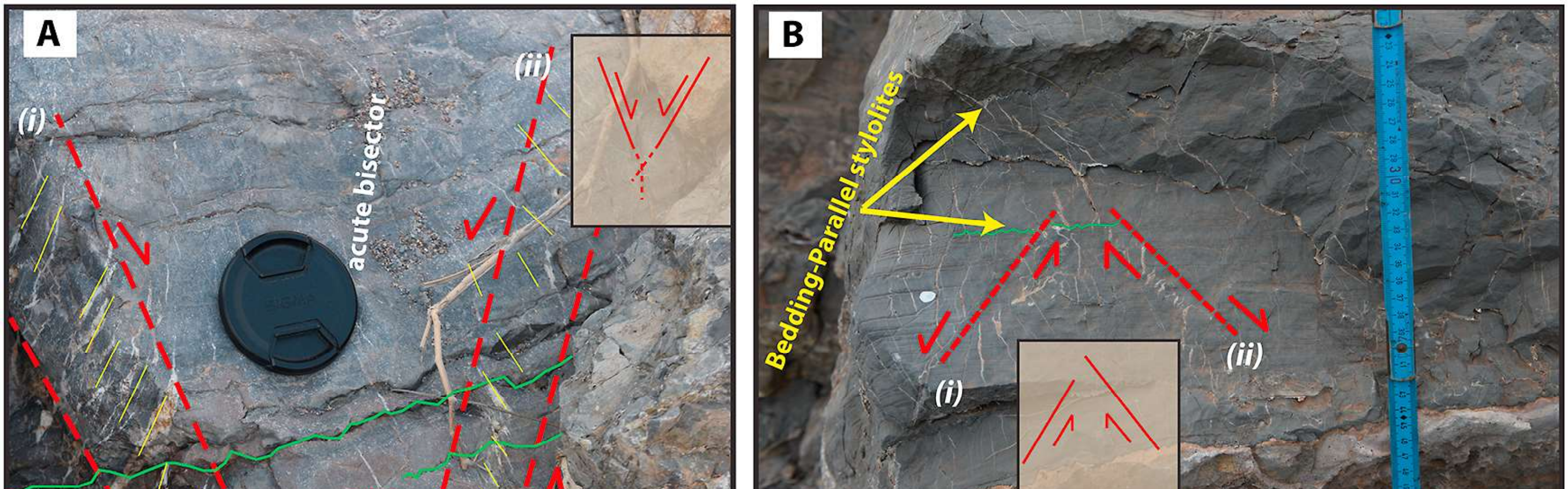

A
(i)
(ii)
acute bisector
Stylolites
Stylolites
Slickolites
Barren joint
Late dolomitic vein
B
Bedding-Parallel stylolites
(i)
(ii)
C
shear zone
en enchelon veins
Stylolites
Sub-vertical veins
(i)
(ii)
Fig. 8E
en enchelon veins
15 cm

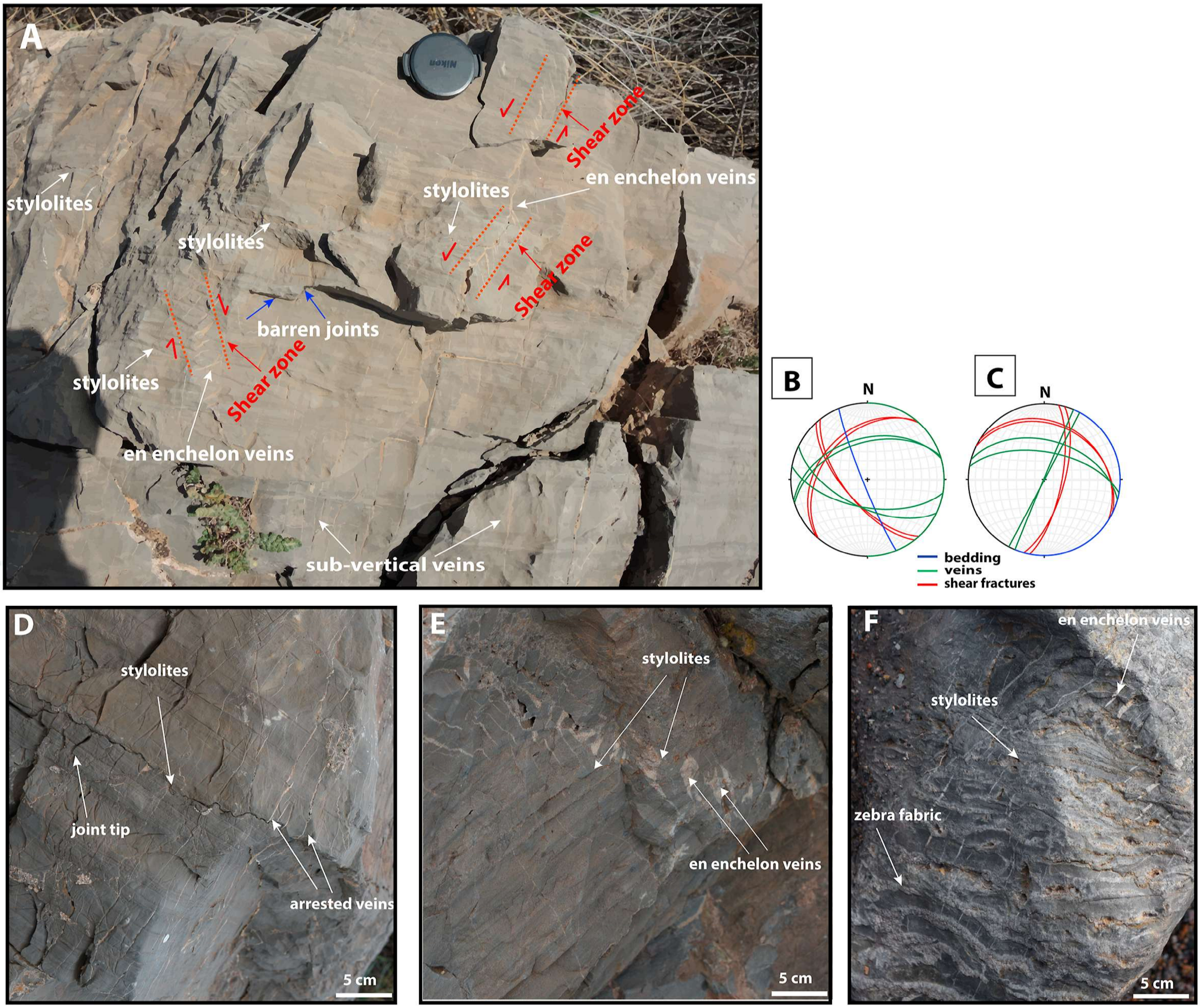

A
stylolites
stylolites
stylolites
stylolites
en enchelon veins
en enchelon veins
Shear zone
Shear zone
Shear zone
barren joints
sub-vertical veins
B
C
N
N
bedding
veins
shear fractures
D
stylolites
joint tip
arrested veins
5 cm
E
stylolites
en enchelon veins
5 cm
F
en enchelon veins
stylolites
zebra fabric
5 cm

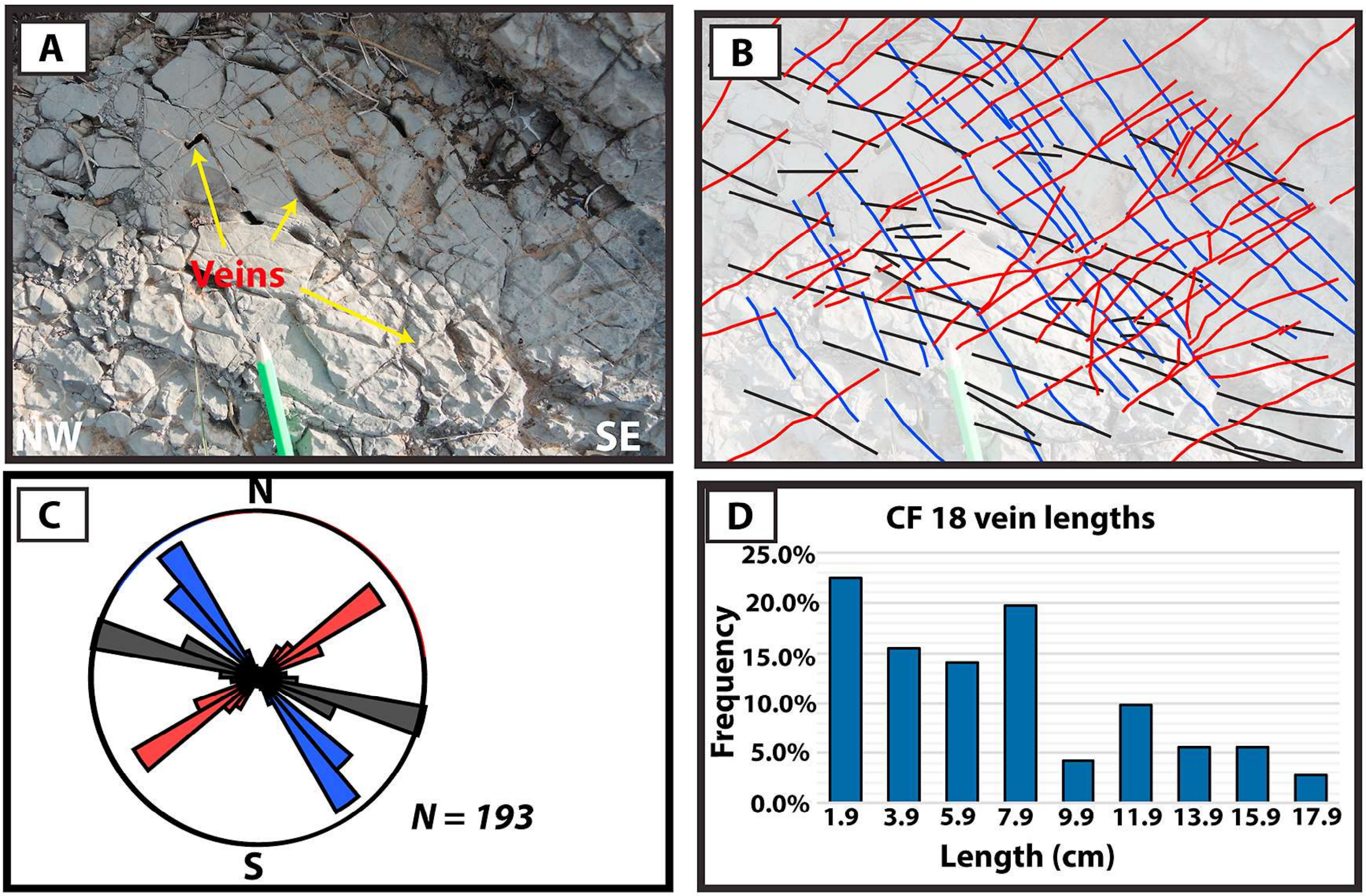

A
Veins
NW
SE
B
C
N
S
N = 193
D
CF 18 vein lengths
Frequency
25.0%
20.0%
15.0%
10.0%
5.0%
0.0%
1.9
3.9
5.9
7.9
9.9
11.9
13.9
15.9
17.9
Length (cm)

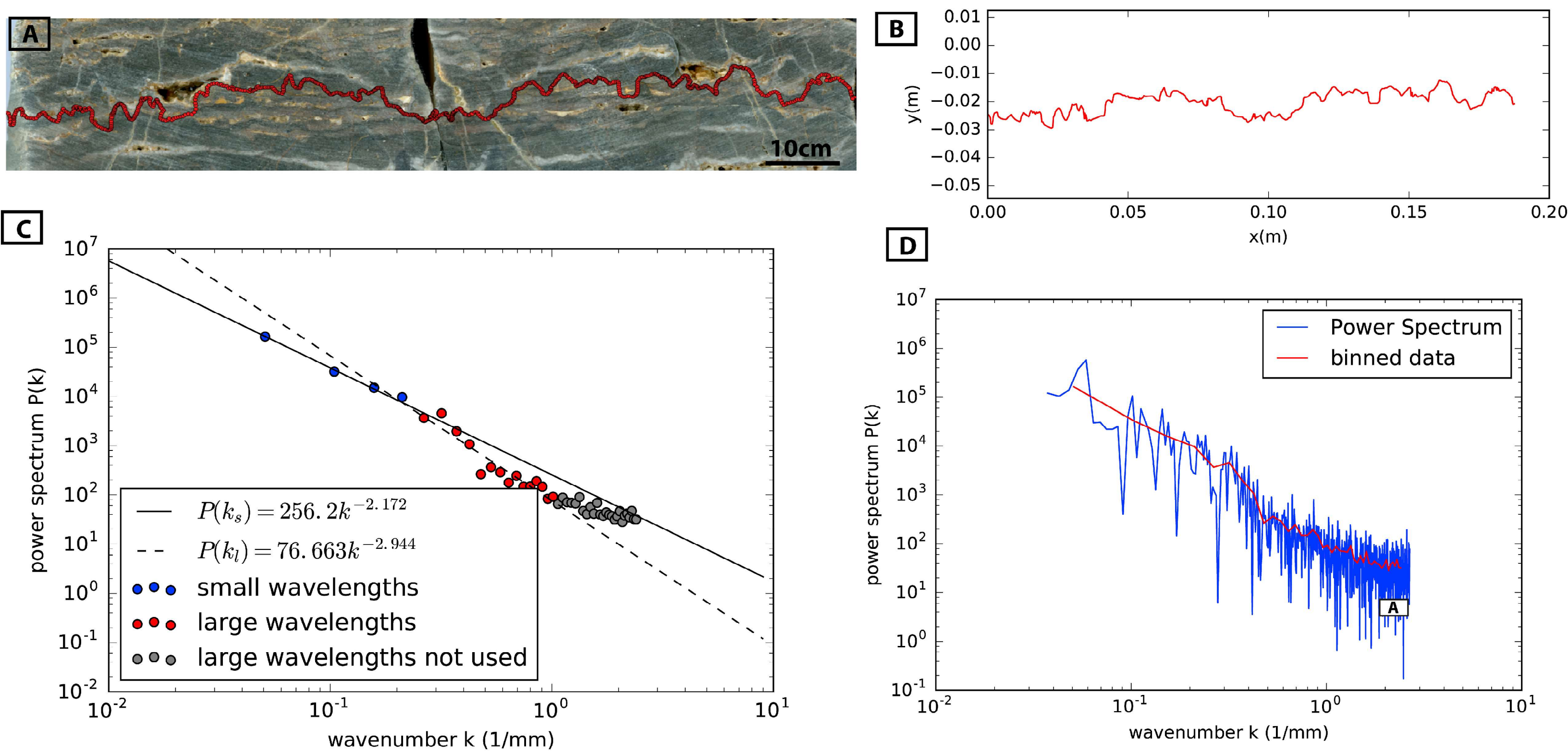
A
10cm
B
y(m)
x(m)
0.01
0.00
−0.01
−0.02
−0.03
−0.04
−0.05
0.00
0.05
0.10
0.15
0.20
C
power spectrum P(k)
wavenumber k (1/mm)
$P(k_s) = 256.2k^{-2.172}$
$P(k_l) = 76.663k^{-2.944}$
small wavelengths
large wavelengths
large wavelengths not used
D
power spectrum P(k)
wavenumber k (1/mm)
Power Spectrum
binned data
A

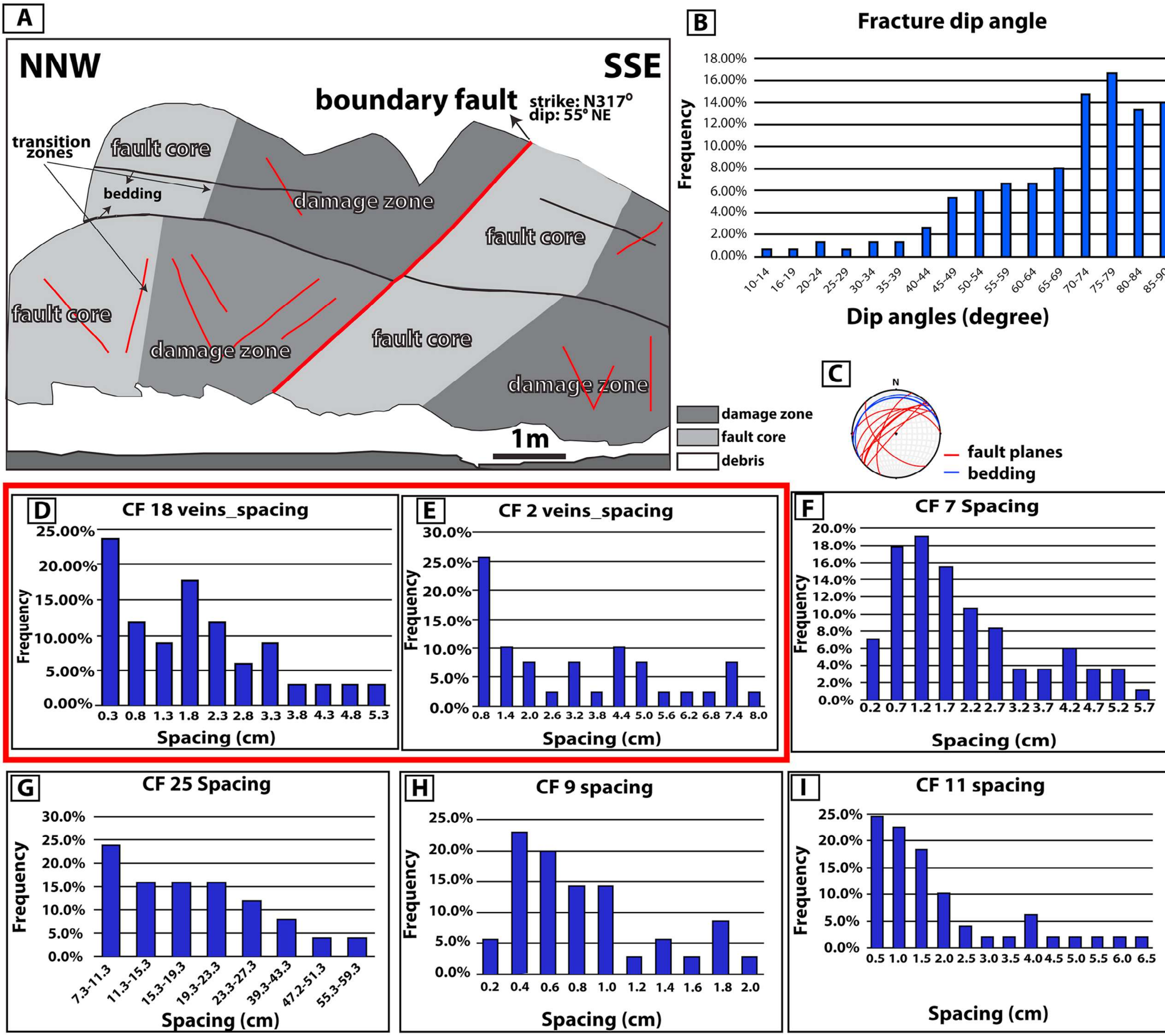
A
NNW
SSE
boundary fault
strike: N317°
dip: 55° NE
transition zones
fault core
bedding
damage zone
fault core
fault core
damage zone
fault core
damage zone
1m
damage zone
fault core
debris
B
Fracture dip angle
Frequency
Dip angles (degree)
C
N
fault planes
bedding
D
CF 18 veins_spacing
Spacing (cm)
E
CF 2 veins_spacing
Spacing (cm)
F
CF 7 Spacing
Spacing (cm)
G
CF 25 Spacing
Spacing (cm)
H
CF 9 spacing
Spacing (cm)
I
CF 11 spacing
Spacing (cm)

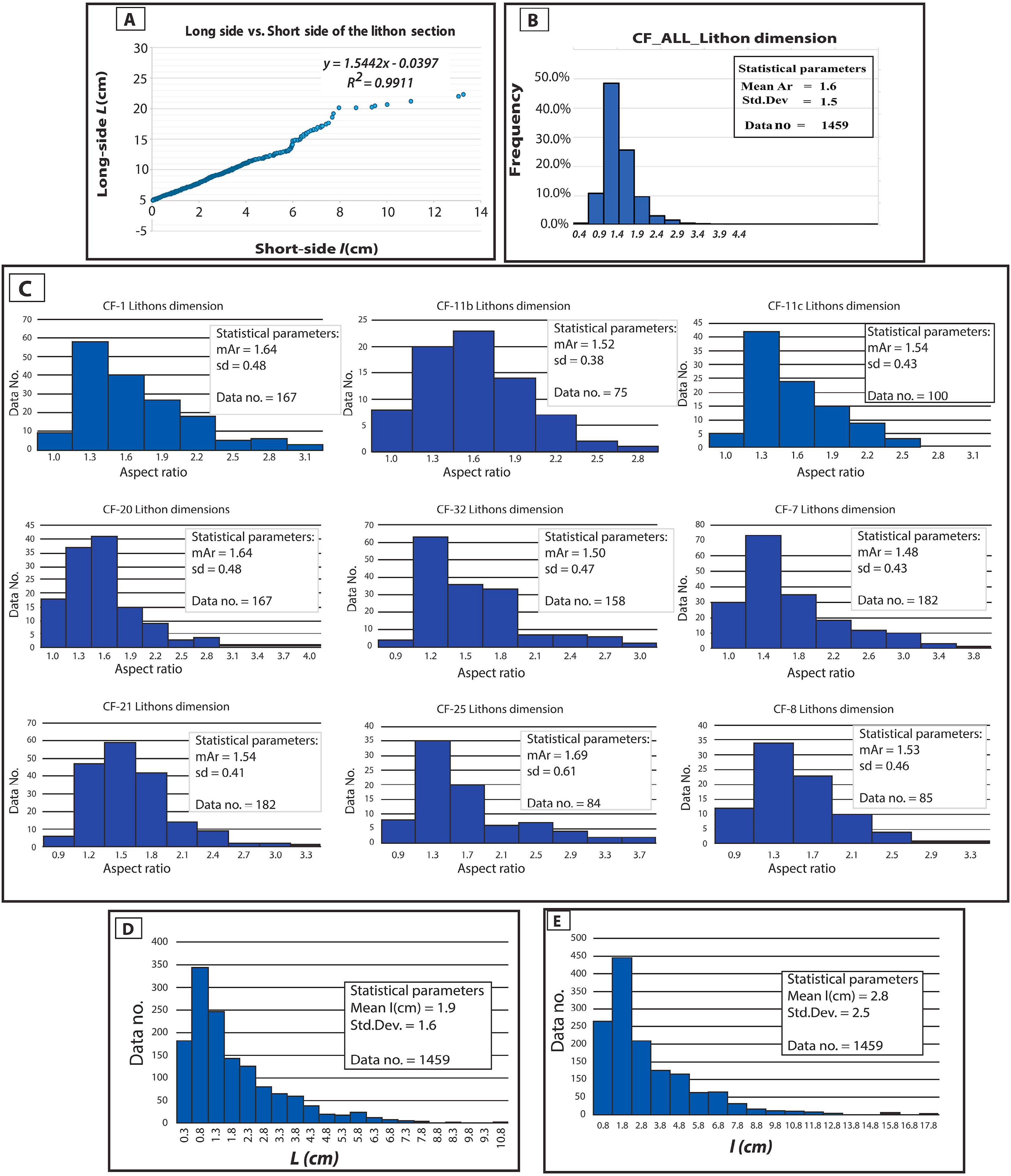
A
Long side vs. Short side of the lithon section
y = 1.5442x - 0.0397
R2 = 0.9911
Long-side L (cm)
Short-side l (cm)
B
CF_ALL_Lithon dimension
Statistical parameters
Mean Ar = 1.6
Std.Dev = 1.5
Data no = 1459
Frequency
C
CF-1 Lithons dimension
Statistical parameters:
mAr = 1.64
sd = 0.48
Data no. = 167
CF-11b Lithons dimension
Statistical parameters:
mAr = 1.52
sd = 0.38
Data no. = 75
CF-11c Lithons dimension
Statistical parameters:
mAr = 1.54
sd = 0.43
Data no. = 100
CF-20 Lithon dimensions
Statistical parameters:
mAr = 1.64
sd = 0.48
Data no. = 167
CF-32 Lithons dimension
Statistical parameters:
mAr = 1.50
sd = 0.47
Data no. = 158
CF-7 Lithons dimension
Statistical parameters:
mAr = 1.48
sd = 0.43
Data no. = 182
CF-21 Lithons dimension
Statistical parameters:
mAr = 1.54
sd = 0.41
Data no. = 182
CF-25 Lithons dimension
Statistical parameters:
mAr = 1.69
sd = 0.61
Data no. = 84
CF-8 Lithons dimension
Statistical parameters:
mAr = 1.53
sd = 0.46
Data no. = 85
Data No.
Aspect ratio
D
Statistical parameters
Mean l(cm) = 1.9
Std.Dev. = 1.6
Data no. = 1459
Data no.
L (cm)
E
Statistical parameters
Mean l(cm) = 2.8
Std.Dev. = 2.5
Data no. = 1459
Data no.
l (cm)

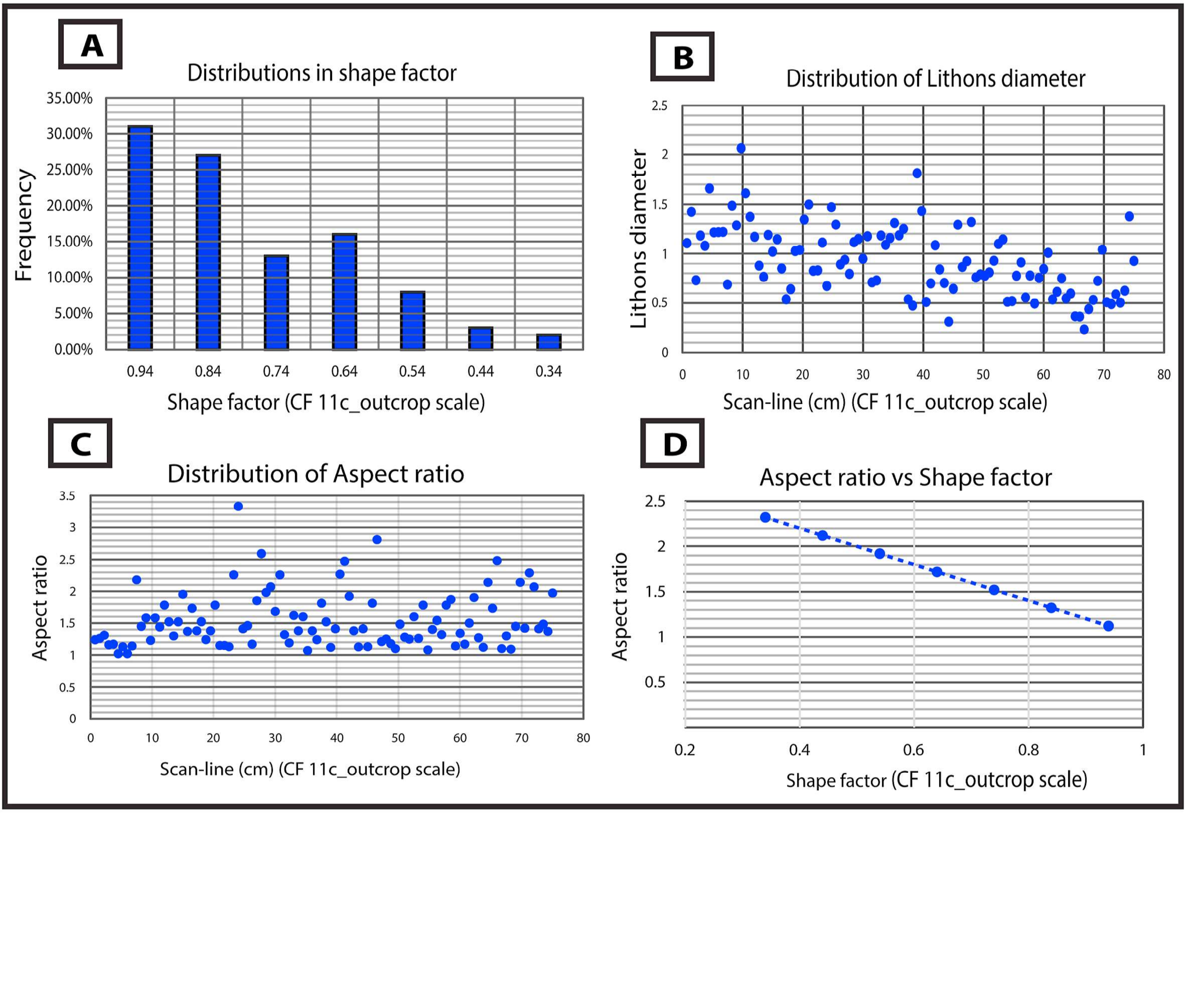
A
Distributions in shape factor
Frequency
35.00%
30.00%
25.00%
20.00%
15.00%
10.00%
5.00%
0.00%
0.94
0.84
0.74
0.64
0.54
0.44
0.34
Shape factor (CF 11c_outcrop scale)
B
Distribution of Lithons diameter
Lithons diameter
2.5
2
1.5
1
0.5
0
0
10
20
30
40
50
60
70
80
Scan-line (cm) (CF 11c_outcrop scale)
C
Distribution of Aspect ratio
Aspect ratio
3.5
3
2.5
2
1.5
1
0.5
0
0
10
20
30
40
50
60
70
80
Scan-line (cm) (CF 11c_outcrop scale)
D
Aspect ratio vs Shape factor
Aspect ratio
2.5
2
1.5
1
0.5
0.2
0.4
0.6
0.8
1
Shape factor (CF 11c_outcrop scale)

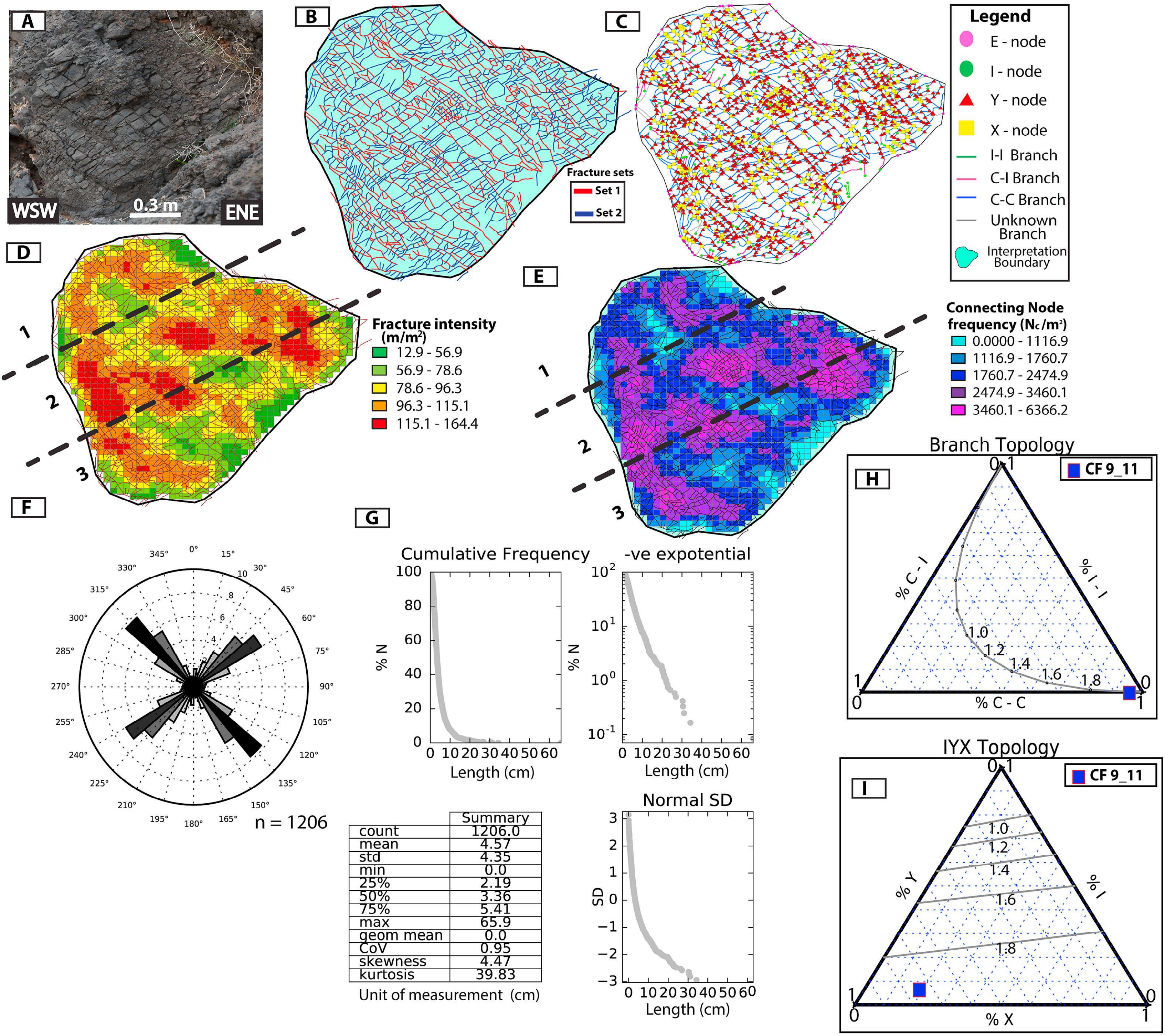

A
WSW
0.3 m
ENE
B
Fracture sets
Set 1
Set 2
C
Legend
E - node
I - node
Y - node
X - node
I-I Branch
C-I Branch
C-C Branch
Unknown Branch
Interpretation Boundary
D
Fracture intensity (m/m²)
12.9 - 56.9
56.9 - 78.6
78.6 - 96.3
96.3 - 115.1
115.1 - 164.4
E
Connecting Node frequency (Nc/m²)
0.0000 - 1116.9
1116.9 - 1760.7
1760.7 - 2474.9
2474.9 - 3460.1
3460.1 - 6366.2
F
n = 1206
G
Cumulative Frequency
-ve expotential
Normal SD
% N
SD
Length (cm)
Summary
count 1206.0
mean 4.57
std 4.35
min 0.0
25% 2.19
50% 3.36
75% 5.41
max 65.9
geom mean 0.0
CoV 0.95
skewness 4.47
kurtosis 39.83
Unit of measurement (cm)
Branch Topology
H
CF 9_11
% C - I
% I - I
% C - C
IYX Topology
I
CF 9_11
% Y
% I
% X

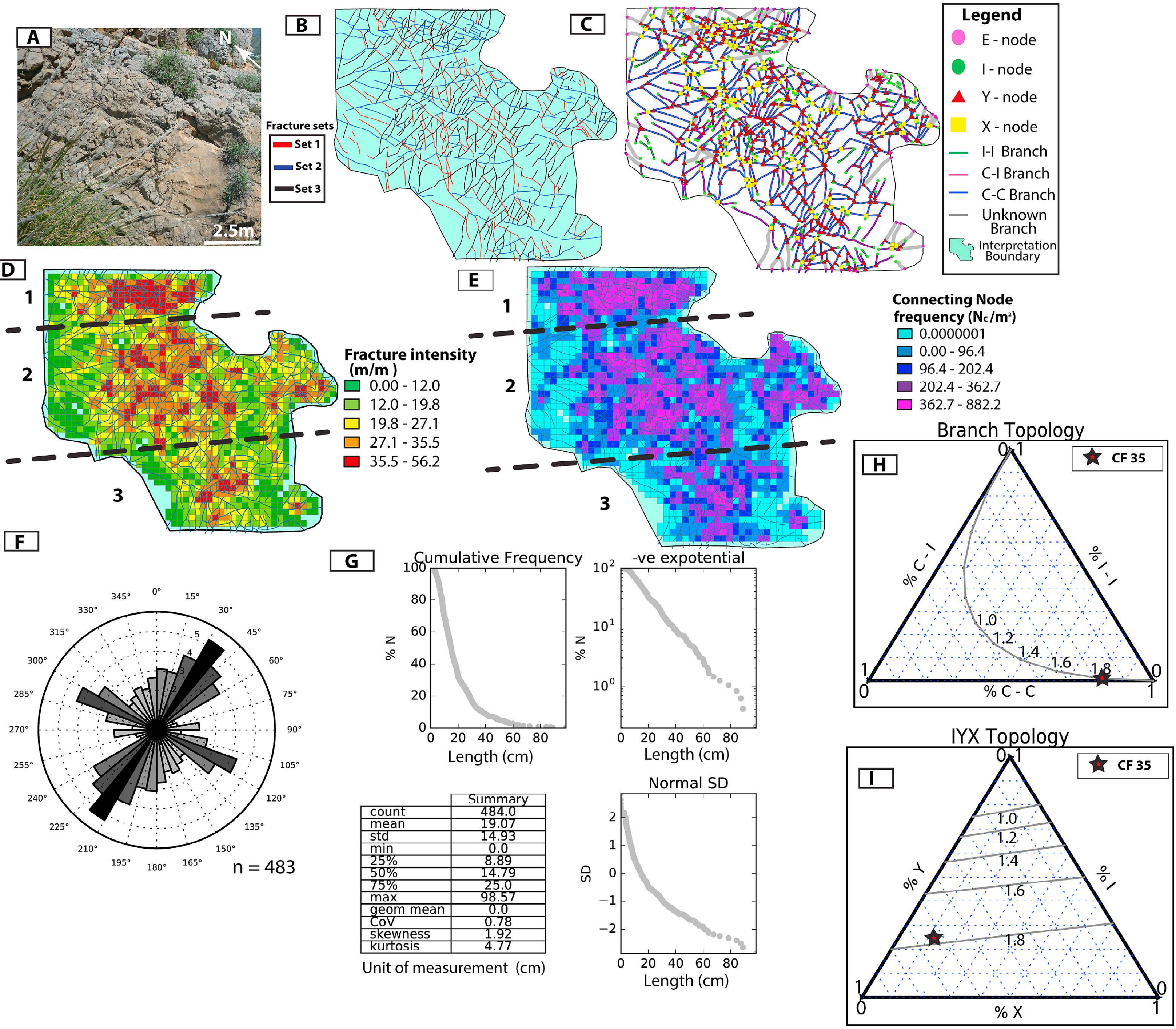

	Summary
count	484.0
mean	19.07
std	14.93
min	0.0
25%	8.89
50%	14.79
75%	25.0
max	98.57
geom mean	0.0
CoV	0.78
skewness	1.92
kurtosis	4.77

Unit of measurement (cm)

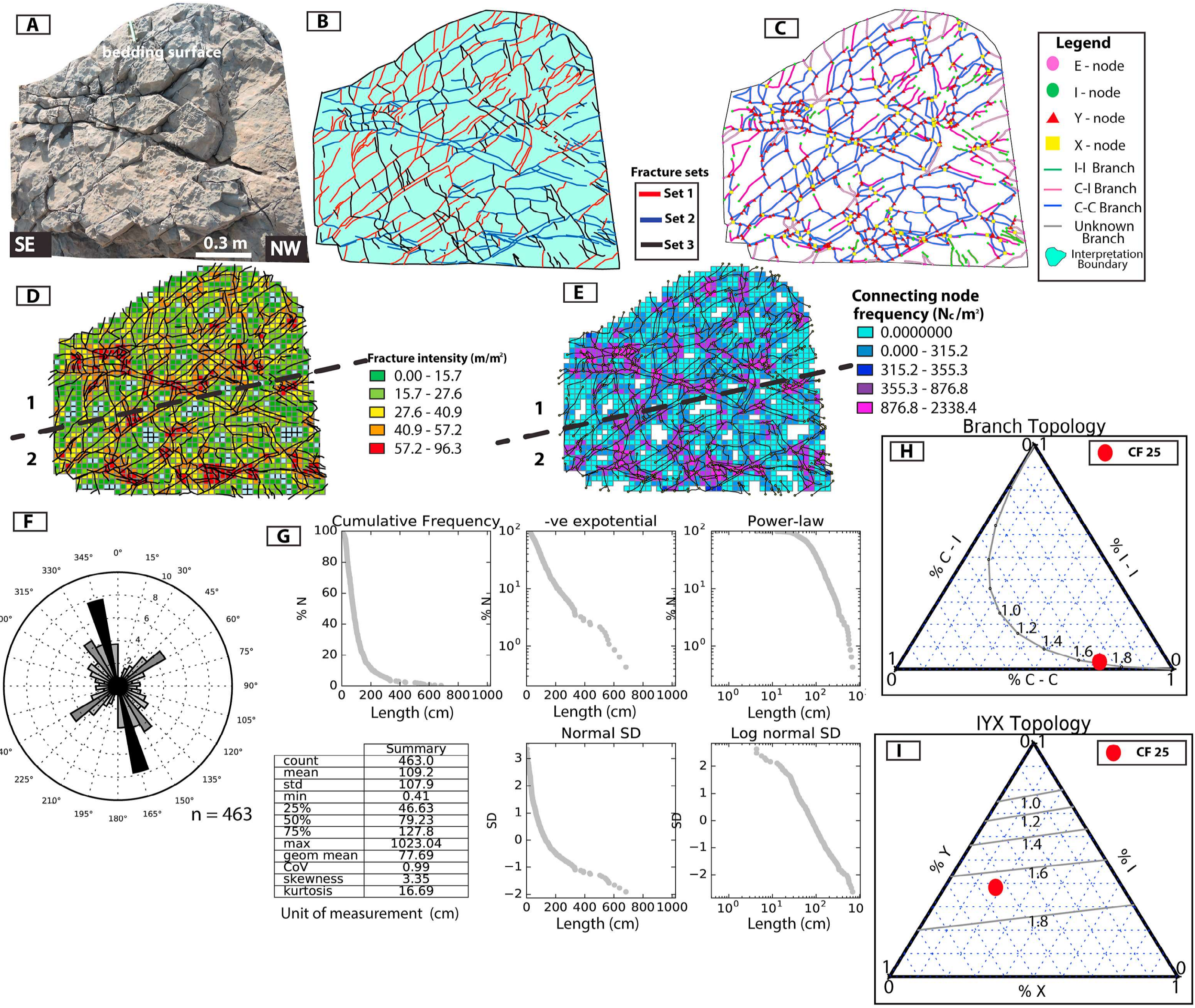
A
bedding surface
SE
0.3 m
NW
B
Fracture sets
Set 1
Set 2
Set 3
C
Legend
E - node
I - node
Y - node
X - node
I-I Branch
C-I Branch
C-C Branch
Unknown Branch
Interpretation Boundary
D
Fracture intensity (m/m²)
0.00 - 15.7
15.7 - 27.6
27.6 - 40.9
40.9 - 57.2
57.2 - 96.3
1
2
E
Connecting node frequency (Nc/m²)
0.0000000
0.000 - 315.2
315.2 - 355.3
355.3 - 876.8
876.8 - 2338.4
F
n = 463
G
Cumulative Frequency
-ve expotential
Power-law
Normal SD
Log normal SD
% N
SD
Length (cm)
Summary
count 463.0
mean 109.2
std 107.9
min 0.41
25% 46.63
50% 79.23
75% 127.8
max 1023.04
geom mean 77.69
CoV 0.99
skewness 3.35
kurtosis 16.69
Unit of measurement (cm)
Branch Topology
H
CF 25
% C - I
% I - I
% C - C
IYX Topology
I
CF 25
% Y
% I
% X

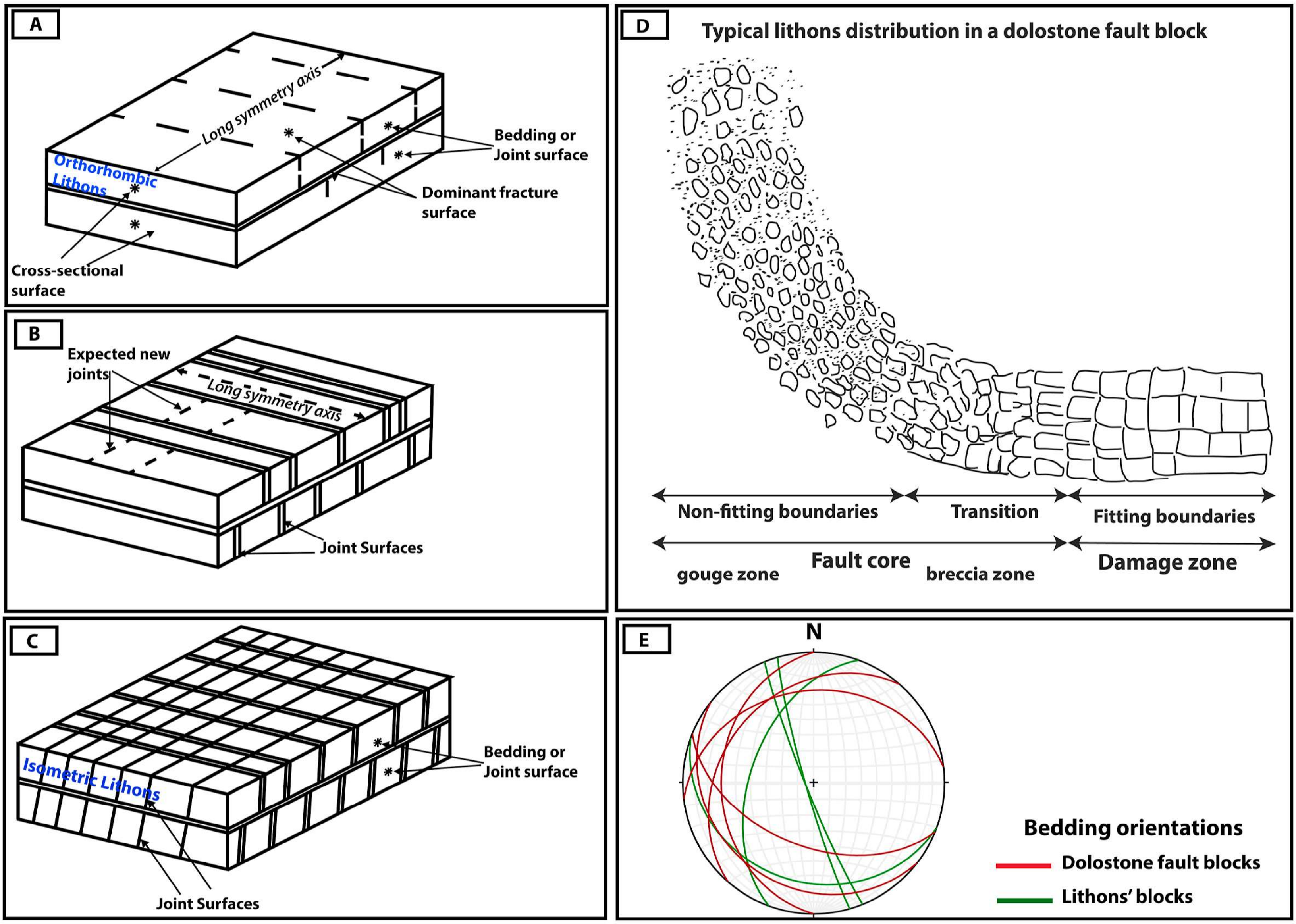
A
Long symmetry axis
Orthorhombic Lithons
Bedding or Joint surface
Dominant fracture surface
Cross-sectional surface
B
Expected new joints
Long symmetry axis
Joint Surfaces
C
Isometric Lithons
Bedding or Joint surface
Joint Surfaces
D
Typical lithons distribution in a dolostone fault block
Non-fitting boundaries
Transition
Fitting boundaries
gouge zone
Fault core
breccia zone
Damage zone
E
N
Bedding orientations
Dolostone fault blocks
Lithons' blocks